A numerical study on the influence of curvature ratio and vegetation density on a partially vegetated U-bend channel flow

Mingyang Wang[1], Eldad Avital[*,1], Theodosius Korakianitis[2], John Williams[1,3], Kaiming Ai[4],

1. School of Engineering and Material Science, Queen Mary, University of London, UK
2. Park College of Engineering, St Louis University, USA
3. State Key Laboratory of Hydraulics and Mountain River Engineering, Sichuan University, China
4. Institute for Turbulence-Noise-Vibration Interactions and Control, Harbin Institute of Technology, China

Abstract

Aquatic vegetation dramatically shifts the main flow, secondary flow and turbulent structures in a meandering channel. In this study, hydrodynamics in a bending channel with a vegetation patch (VP) has been numerically studied under the variation of curvature ratios (*CRs*=0.5, 1.0, 1.5, 2.0) and the vegetation density i.e. Solid Volume Fractions (SVF=1.13%, 4.86%). Both effects on vegetation shear flow, helical flow, bed shear stress and bulk drag coefficients are studied in twelve cases by using Ansys Fluent package. Unsteady Reynolds Averaging Navier-Stokes (URANS) framework coupled with the Reynolds Stress turbulence Model (RSM) and Volume Of Fluid (VOF) approach is successfully applied to predict the entire flow field including multi-circulation cells as well as the free surface. The conclusions are summarized as three points. Firstly, an increase of *CR* moves the main circulation cell and thalweg's location towards the outer bank, while decreasing the drag coefficients in streamwise and spanwise. However, the *CR* weakly affects the normalised shear flow velocity profiles and dominant eddy frequencies downstream of the VP. Secondly, the trend of the dominant shedding frequency to fall with the increase of SVF that has been known only for SVF<3.4% is extended up to 10.4%. Furthermore, an opposite trend is found between the frequency and SVF for 10.4%<SVF<20%. Thirdly, a newly proposed patch

dimensionless frequency number, $St_p\frac{\sqrt{\mathrm{SVF}}}{\sqrt{N}}$, links St_p and SVF, where N is the number of stems in the patch. This number stays almost constant for each case series regardless of the variation of SVF (for SVF<10.4%). We also conclude that $St_p\frac{\sqrt{\mathrm{SVF}}}{\sqrt{N}}$ is strongly determined by the patch shape factor, mildly influenced by the patch Reynolds number, but it excludes the influence of the SVF and N. The insights from the present study unveil the complicated eco-hydro-morphic interactions among the bio-mass density, turbulent flow and channel meanders' variation. It provides a better understanding of natural bending river systems' development and fundamentals for the recovery of urban channel ecosystems by vegetated re-meandering.

Keywords: Vegetation patch (VP) flow; U-bend channel; Helical flow; Curvature ratio (*CR*); Solid volume fraction (SVF); Drag coefficient;

1.Introduction

Meandering rivers with vegetation patch (VP) are ubiquitous in nature. The turbulent flow fields in curved channels is quite complicated, controlled by channel's meander and vegetation's obstruction. These two factors also significantly alter the morphology of rivers by redistributing the bed shear stress and inducing erosion events (Chen et al., 2012) and sedimentation events (Armanini and Cavedon, 2019). The effects of these two factors are separately reviewed in the following two paragraphs.

In a flat-bed (non-vegetated) open channel, the channel bending effects on flow structures and bed shear stress have been extensively explored in previous researches. It was found that varying the river or channel curvature ratio (*CR*) shifts the secondary flow, where the *CR* is defined as a *B/R*, where *R* is inner bank radius of channel bends and *B* is the width of channel. Kashyap et al. (2012) and Zimmermann (1977) concluded that decrease both *CR* and the *B/H* (channel width/flow depth) strongly improved the secondary flow circulation strength in a flat-bed channel, where the circulation strength was defined as a surface integration of the streamwise vorticity. In their case of a 135-degree flat bending channel with *B/H*=5, there was around 33% augmentation in the circulation strength, when *CR* reduced from 3.0 to 1.5. Nonlinear one-dimensional (1D) analytical models were proposed and verified (Wei et al., 2016, Blanckaert, 2011) to illustrate the relationship between *CR* and the magnitude of secondary flow. Secondly, the location of the maximum bed shear stress in each cross-section of the bending channel bed shifts from the inner bed to the outer bed along the entire meandering region. That is because the bending effect redistributes the main flow and alters the maximum velocity gradients' location. Thirdly, in tight bends, *CR*<3, secondary flows of double-cell circulations are observed in regions after the bend's apex. In those regions, the main circulation cell is generated from the non-equilibrium of the centrifugal force and the transverse pressure gradient, while the outer-bank cell close to the upper area is formed from the Reynolds stress distribution (Kashyap et al., 2012, Blanckaert and De Vriend, 2004).

The presence of VP significantly affects the flow dynamics in river beds. In a short term, VP reduces discharge capacity, converts the mean kinetic energy to turbulent kinetic energy in plant stem scales (Nepf, 2012, 1999,) and redistributes the bed shear stress (Chen, et al., 2012). Schnauder and Sukhodolov (2012) pointed that the bed surface shear stresses have a significant increase on the lateral side of the VP, since the VP squeezes the flow and speeds up the velocity in the neighbour non-vegetated region. In a long term, the presence of the VPs has an essential role in the evolution of the river basin geomorphology (Wu et al., 2005) and promotion of bends' migration (Zen et al., 2016) by promoting sedimentation in point bar.

Only a small number of numerical studies predicted the vegetation flow in meandering channels while accounting for the 3-dimensional (3D) flow characteristics, especially the secondary flow. Most researchers achieved vegetation-hydraulics-morphology interactions by using 2-dimensional (2D) numerical models, focusing on distinctive factors, such as the VP evolution (Jourdain et al., 2020), geomorphology development (Bywater-Reyes et al., 2018, Crosato and Saleh, 2011, Wu et al., 2005), channel bed strengthening by roots (Caponi and Siviglia, 2018), seasonal floods (Kang et al, 2018) as well as bank stability (Asahi et al., 2013, Eke et al., 2014).

However, those 2D model-based studies mostly employed the shallow water equations and ignored secondary flow effects, which would introduce inaccuracies to flow pattern distribution and morphological prediction. Also, the 2D model can highly overpredict the skin friction of a channel bed. The previous study divided the total bed stresses into skin friction, the drag from plants and the drag of bed morphology (Le Bouteiller and Venditti, 2015). Many 2D models often consider the skin friction only, and thus artificially increase the skin friction coefficient to account for the drag effects of the plants and bed morphology (Bywater-Reyes et al., 2018, Bertoldi et al., 2014, Camporeale et al., 2013, Nicholas et al., 2013). These models worked well for the velocity reduction in vegetated region, but they smear the turbulent structures both in the plant stem scale and patch size scale which actually governs the dispersion of sediments. Moreover, this overpredicted skin friction can lead to the overestimation of the bedload transportation. In real natural rivers, the presence of vegetation generally decreases the skin friction and bedload transportation rate, as compared to the bare channel bed. Therefore, those aspects mentioned limit the accuracy and reliability of 2D models' prediction.

A 3D Unsteady Reynolds Averaged Navier-Stokes (URANS) numerical method with the isotropic $k-\varepsilon$ turbulent model was firstly adopted by Huai et al (2012) to study the effects of continuous vegetation stripe close to the inner bank of a U-bend channel flow. In comparison with physical results, their numerical predictions agree well with the bed shear distribution and primary flow distribution. However, Van Balen et al., (2010) argued that URANS along with the isotropic $k-\varepsilon$ is limited in mimicking secondary flow structures produced by the anisotropic turbulent flow field in a non-vegetated bending channel. Thereby, in the present study, URANS framework along with an anisotropic turbulent model, Reynolds Stress Model (RSM), is employed to predict the flow field.

Substantial physical experiments (Termini, 2017, Nepf, 2012, Folkard, 2005), and field studies (Schnauder and Sukhodolov, 2012, Armanini et al., 2005) were also conducted to unveil the complicated interactions between the flow pattern, vegetation and geomorphology. In particular, Termini (2017) experimentally found that vegetated layers fully covered the bed could interrupt the flow pattern existing in non-vegetated curved bends, and split the cross-sectional circulation cell into smaller cells. Schnauder and Sukhodolov (2012) pointed out that continuous riparian vegetation modified the velocity profile in the streamwise flow direction and relocated the location of secondary circulation cells. However, almost no systematic efforts have been paid to analyse the interactions between the VP and the secondary flow, under the variance of SVF and *CR*.

The potential implications and applications of this study are as follows: deeper insights into the hydrodynamics of channel bend with partially covered bio-mass are fundamental for river management and ecosystem restoration. In general, the VPs in channel support physical (sedimentation, erosion), chemical (accumulation, sorption) and biological (self-purification, oxygen production and denitrification) processes. For one application, VPs are used to re-meander urban water ways which usually have fewer meanders than natural rivers (Krauze et al., 2008). Re-meandering an urban channel by organizing VPs in it, helps to rebuild the flow pattern to semi-natural characteristics and retrofit naturally-like pool-riffle structures. These structures favour biodiversity by providing variable conditions in river cross-sections (Dale, 1996; Schwartz et al, 2002). As a result, the VPs-planted urban channel systems are provided with ecological functions, better resistance and resilience to overcome anthropogenic impacts. For another application, VPs are used to control the flow direction downstream of a bending channel in short term, while modifying curvature degree or the direction of the bend exit in a soft way in the long term.

In this paper, the following related questions are investigated by employing Ansys Fluent package. A 3D incompressible URANS method coupled with a high-order anisotropic turbulent model, RSM, is chosen to conduct this study:

i) How are the mainstream shear flow and helical flow structures organized, located in the upstream and downstream cross-sections of a VP? What happens when the channel bend becomes tighter as well as the SVF increases?

ii) What are the redistribution characteristics of the channels' bed shear stress under the variation of bend *CR* and VP blockage effects?

iii) What are the physical characteristics of force coefficients (C_d) of VP and dominant frequencies of vortices' shedding under the variation of *CR* and SVF? What is the quantitative relationship between those variables? What is the dimensionless frequency number of VP when excluding the effects of the number of stems and SVF?

This paper is organized in the following way: The numerical model and the set-up of simulations are described in section 2. Validation of flow patterns and the accuracy of the drag predictions are discussed in section 3. Section 4 carefully discusses the three groups of related questions aforementioned, followed by conclusions in section 5. Nomenclature is displayed in section 6, and the supplementary materials relevant to validation is demonstrated in section 7.

2 Model description

2.1 Flow geometries and dimensions

Dijk et al. (2013) pointed out that aquatic VP had a higher possibility of growing in the inner bank than the outer bank. This is because many aquatic species in nature are transported hydrochorously, i.e., by flowing water. This physical process includes the seeds being dispersed by nautohydrochory, i.e., at the water surface and by the bythisochory, i.e., by spiral (secondary) flow at the bottom of channel, which is illustrated in Fig.1. This secondary flow direction pushes the seeds up to the inner bank beach while dragging seeds into the river from the outer bank (Merritt and Wohl, 2002; Gurnell et al., 2008). The natural river inner bank slope is usually slower/gentler than the outer bank. As a result, the seeds are more likely stranding in the inner beach and germinate while other conditions are suitable. For instance, the Tollense river located in north-east Germany, in which more vegetation thrives in the inner bank than outer bank after the apex, was investigated by Schnauder and Sukhodolov (2012). Also, quite more vegetation located in the inner bank than the outer bank in the meandering river Koyukuk, Alaska (Van Dijk, 2013).

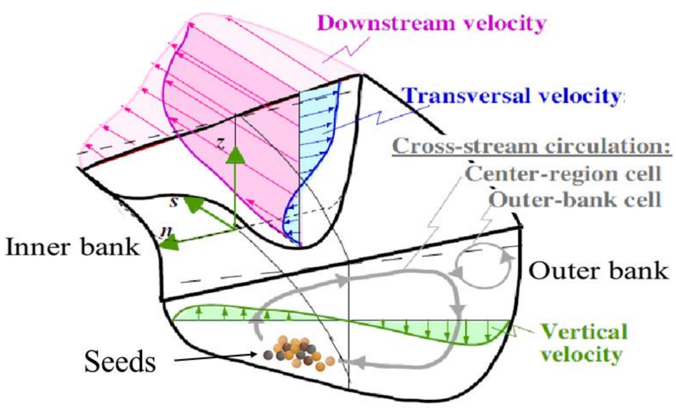

Fig.1 A sketch of seeds transport and secondary flow structures in a bending channel in nature (This sketch is created based on Graf and Blanckaert, 2002). The secondary flow structures include the main circulation cell, which carries the seeds on the inner bank, and the outer-bank cell.

Moreover, VP in the apex of inner bank facilitates the morphological development of point bar and extensive studies have focused on this location, but a very limited research illustrates the effects of VP in the exit of the bend even through the VP sometimes thrives there. The exit of the U-bend channel also experiences a strong circulation of secondary flow (Huai et al., 2012) and ties the bending channel and downstream straight channel region. VPs at the exit of U-bend channel can also influence the development of a point bar and morpho-dynamics, but very few previous studies related to this question. Therefore, we designed the VP in the inner bank of U-bend channel, and also examined whether the presence of an emergent VP in the exit can diminish or eliminate the helical flow that affect river management.

The experimental conditions in a curved vegetated channel found in literature are listed in Table 1, which will act as comparisons to the present design of geometries and dimensions. The present simulation geometries and the vegetation canopy arrangement mainly refer to the geometry of the laboratory flume from Huai et al. (2012), but the range of other features like *CR* and *B/H* are designed in a reasonable range referring to other studies in Table 1. Overall, in order to isolate the influence of the *CR* and SVF on the curved channel flow, the single fixed-flat U-bend channel with emergent stems are designed along the inner bank, which is shown in Figs.2(a)(b).

Table 1. Experimental conditions in 3D curved vegetated channels in literature

	Channel shape	Vegetation condition	Bed conditions	*CR*	*B/H*
Huai et al., (2012)	Single U-bend	Emergent, partially cover inner bend	Fixed-flat bed	1.5	6.7
Termini, (2017,2018)	Multi-sine shape	Submergent, cover full bend	Mobile-uneven bed	1.44 at apex	9.6
Hamidifar et al., (2019)	Multi-sine shape	Emergent, partially cover outer bend	Mobile-uneven bed	2.1 at apex	2.0
Yang et al., (2019)	Single U-bend	Emergent, partially cover outer bend	Fixed-flat bed	1.5	6.7
Farzadkhoo et al., (2019)	Multi-sine shape	Emergent, partially cover inner bend	Fixed-flat compound channel bed	1.0	2.4

In this study, each bending channel consists of a 4-meter straight inflow/outflow channel and a 180-degree curved channel section with an inner bank radius, R=0.5~2.0. Eight vegetated U-bend cases with different *CRs* (0.5, 1.0, 1.5 and 2.0), SVF*s* (1.13%, 4.86%) and four non-vegetated U-bend cases were used to conduct this parametric study. To exclude influence from other factors, and to isolate the three factors of *CR*, SVF and VP, all other parameters of the twelve geometries were kept the same. These parameters include the width of the bending channel (B=1 m), the discharge rate of the inflow (Q=0.03 m^3/s), the depth of the outlet water 0.148m and the relative position of the VPs (Figs.2(a)(b)). The total depth of the computational domain is 0.216m. Those settings refer to the laboratory experiments of Huai et al. (2012). All the information about the twelve study cases are shown in Table 2.

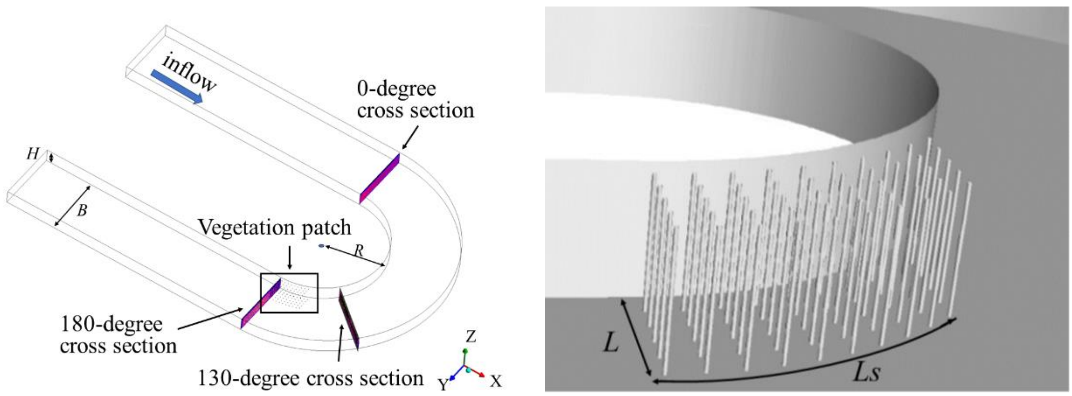

(a) (b)

Fig.2 (a)The schematic of a bending channel with a VP. The VP is in the box region where is the exit of bend close to the inner bank. Three cross-sections are plotted in this picture, the physical variables of the flow will be plotted in these cross-sections in the following sections. Key parameters of the inner bank radius, *R*, the width of channel, *B*, the height of channel, *H*, are marked on this figure. (b) The zoom-in view of VP, where the spanwise length of VP, *L*, and streamwise length *Ls* are marked on it.

The locations of VPs were controlled by fixing the final row of cylindrical stems at the 180-degree cross-section. The diameters of those stems are 6mm or 12.45mm, and the distance between each stem in the streamwise and spanwise direction is 50mm. Thus, the spanwise dimension (L) and streamwise dimension (Ls) are 0.25m and 0.45m, respectively. Note that the ratio between the width of channel (B) and the spanwise dimension of VP (L) can be regarded as a “relative submergence”, B/L in the spanwise direction. The coherent turbulent motion along the VP’s lateral interface is quite sensitive to B/L (Termini and Di Leonardo, 2018), but the influence of this factor for bending channel is beyond the scope of current study. Therefore, B/L is kept at 4 for all cases in the present study. Illustrations are given in Figs.2(a)(b) and Figs.3(a)(b) for the geometries of the emergent canopies and the computational meshes around the canopies.

Table 2. All study cases details

Cases	*R*(m)	*CR*	SVF	*d*(mm)	Re_d
1	0.5	0.5	1.13%	6	1200
2	1	1	1.13%	6	1200
3	1.5	1.5	1.13%	6	1200
4	2	2	1.13%	6	1200
5	0.5	0.5	4.86%	12.45	2490
6	1	1	4.86%	12.45	2490
7	1.5	1.5	4.86%	12.45	2490
8	2	2	4.86%	12.45	2490
9	0.5	0.5	0.00%	0	
10	1	1	0.00%	0	
11	1.5	1.5	0.00%	0	
12	2	2	0.00%	0	

R the radius of the inner bank; *CR* is the curvature ratio (*R/B*); SVF the vegetation density; Re_d is Reynolds number based on the average inlet velocity and the diameter of stems, *d*; *Q* is the inlet flow rate, 0.03(m^3/s); *H* is the depth of channel outlet, 0.148m; *B* is the width of channel 1m. In all cases the value of *Q, H, B* keeps constant.

2.2 Governing equations and turbulence modelling

The incompressible Unsteady Reynolds Averaged Navier-Stokes (URANS) equations (1), (2) were used as the governing equations:

$$\frac{\partial \overline{u}_i}{\partial x_i} = 0, \tag{1}$$

$$\frac{\partial \overline{u}_i}{\partial t} + \overline{u}_j \frac{\partial \overline{u}_i}{\partial x_j} = -\frac{1}{\rho}\frac{\partial \overline{p}}{\partial x_i} + \nu \frac{\partial^2 \overline{u}_i}{\partial x_j \partial x_j} - \frac{\partial \overline{u_i' u_j'}}{\partial x_j} + \overline{f}_i . \tag{2}$$

Ansys Fluent package was used to make those simulations. The high-order URANS model Reynolds Stress Model (RMS) method was used to resolve the Reynolds stress gradient term $\frac{\partial \overline{u_i' u'_j}}{\partial x_j}$; in order to capture the anisotropic effects in the curved channel, such as the outer-bank circulation cells. The common two-equations models like $k-\varepsilon$ and $k-\omega$ can struggle in capturing these effects. However, the RSM model has successfully predicted such anisotropic flows (Kashyap et al., 2012, Ramamurthy et al., 2012, Sugiyama and Hitomi, 2005). RSM also presented a strong capability to predict the turbulent flow with VPs (Choi and Kang, 2004, Souliotis and Prinos, 2011). Furthermore, the URANS RSM approach is computationally less expensive than Large Eddy Simulation (LES), so it was feasible to carry this parametric study using reasonable computational cost.

The RSM, which abandons the Boussinesq hypothesis, solves the transport equations for the six components of the Reynolds stresses separately and the energy dissipation rate (ε or ω) to provide the closure of equations (1) (2) (Launder, et al., 1975, 1989). In this study, we adopted the ω energy dissipation transport equation because of the good performance in laminar boundary layers of stems, considering the Re_d in Table.2. No wall functions were used in this study.

As for the mesh, a mixture of the structured grids and unstructured grids were constructed in the VP areas. The dimensionless of mesh scales, $\Delta r/d$, is 1/15, as shown in Fig.3(b). The maximum grid's near wall spaces in the horizontal plane $(\Delta x^+, \Delta y^+)_{\max}$ are less than 30 units and the maximum vertical dimensionless distance $(\Delta z^+)_{\max}$ between horizontal layers is less than 72 units. In the non-vegetated area far from the VP, the structure grids, $(\Delta x^+, \Delta y^+)_{\max} \approx 500$ units, are adopted. The total number of grids in different cases are 4.9~6.0 million. This meshing resolution is referred to the Braza et al. (1986) and the Huai et al. (2012). More information are presented in the following validation part.

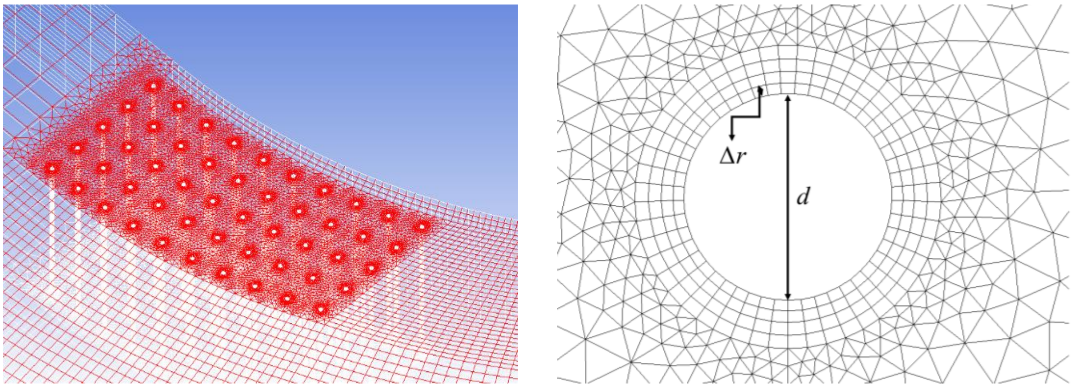

(a) (b)

Fig.3 (a) a mesh of the entire VP in the bending region. (b) a zoom-in view of the mesh of a single stem in that VP. Δr is the distance between the first node to cylinder's surface and d is the diameter of each stem.

2.3 Boundary conditions and discretisation scheme

In order to obtain reliable and physical results, the following boundary conditions are used: The inlet discharge water flow rate is 0.03m^3/s, which is extracted from a fully developed straight open channel with a periodic boundary condition in the streamwise direction. The outlet boundary condition is controlled by the water's depth, 0.148m. The top of the domain is set as the atmospheric pressure outlet. Moreover, the surfaces of the fixed-flat channel bed, side walls and the surfaces of the stems are set as no-slip wall boundary condition.

The second-order Volume of Fluid (VOF) method is used to capture the free surface of water. In previous research, the rigid-lid assumption was adopted in several curved channel flow studies to obtain relatively good results, as long as the Froude number is less than 0.5 (Kashyap et al., 2012, Van Balen et al., 2010), and the water surface elevation is less than 10% of the depth of the channel (Constantinescu et al., 2011). However, a pressure gradient error may still occur owing to the unwanted force from the rigid lid and no water surface elevation difference between the inner bank and the outer bank. Thus, modelling the effects of free surface improves the accuracy of the current simulations (Ramaurthy et al, 2012, Zeng et al., 2006). Ramaurthy even argued that predictions from the RSM combined with VOF are better than that of LES applied with a rigid lid treatment in a 90-degree bending channel flow when compared with experimental results. Furthermore, flow around single cylinder with free surface in large Froude number condition, considering deformation effects of multiphase interface is critical (Yu et al., 2008). Therefore, the free surface elevation was taken into consideration and simulated.

The Semi-Implicit Method for Pressure Linked Equations-Consistent (SIMPLEC) scheme was adopted as the time marching method to ensure convergence and stability. The SIMPLEC's skewness corrections reduce the errors generated at the interfaces between structured grids and unstructured grids. A relatively low under-relaxation value of 0.15 was set in the momentum equations to stabilise the RSM model which is more sensitive and easier to diverge as compared to $k-\varepsilon$ and $k-\omega$ models.

Second-order implicit scheme was employed to discrete key terms while using the Bi-Conjugate Gradient Stabilized Method (BCGSTAB) solver for the Poission equation. The second-order upwind scheme was chosen to discrete the momentum terms and the turbulent dissipation terms. Power-law differencing scheme was used to discretise Reynolds stress terms to keep the stability of the turbulence model. This differencing scheme was already successfully used in vegetation flow prediction (RSM) (Kang and Choi, 2006). The maximum Courant Number was set as 0.5 in order to avoid under-predicting the forces exerting on the stems array when using improper large time steps.

3. Validation

3.1 Flow pattern validation

The U-bend open channel with vegetation stripe in Huai's study case (Huai et al. 2012), displayed in Fig.4, is similar to the present geometry shown in Figs.2(a)(b), and the only difference is the streamwise length of the VP. Thus, the experimental data published by Huai was used to verify the capacity of the selected numerical method, 3D URANS RSM VOF. This numerical-model-test mesh is based on the Huai's experimental geometry with the same boundary layer fineness and average resolution to the twelve meshes of the present study cases (shown in Table 2). The selected numerical model and the selected numerical schemes mentioned before were adopted on this numerical-model-test mesh to obtain the numerical prediction results. The locations of the velocity profile sample points (a~i) are shown in Fig.4. The mean streamwise velocity profiles at those locations are shown in Fig.5.

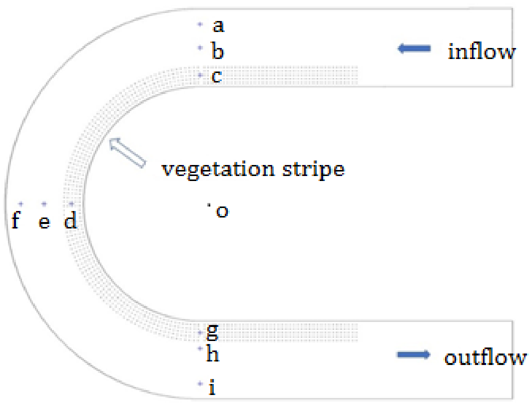

Fig.4 The experimental geometry of Huai et al. (2012). The numerical-model-test mesh is constructed on this geometry. This geometry is used for the selected numerical model validation. Points a~i are the locations of the vertical velocity profiles shown in Fig.5.

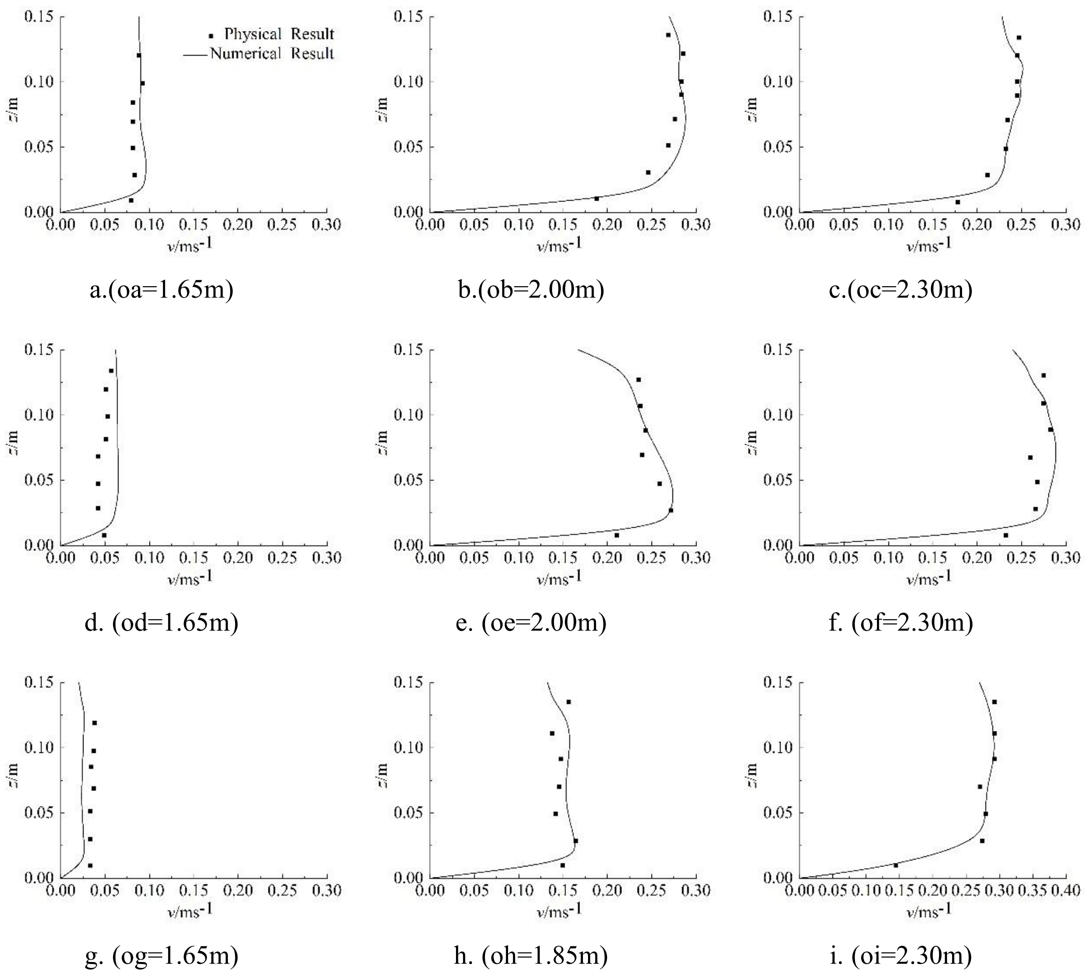

Fig.5 Comparisons of the mean streamwise velocity profiles between the numerical results (solid lines) and measured physical results (squares). The distance between the bend centre point o to sample location a is expressed as oa in Fig.5a. Distances for other sample locations are expressed in the similar way.

Good agreements were achieved between the numerical and physical results in most locations, which demonstrates that the current numerical model is properly chosen and the turbulent model constants are well defined to predict the current turbulent flow pattern with a streamline curvature and a separation region. The values of those model constants follow the recommendations in Table 3 (Ansys Fluent Theory Guide, 2019).

Table 3 the constants for RSM adopted in the present research

constant	C1	C2	α_∞^*	α_∞	α_0	β_∞^*	β_l
value	1.8	0.52	1	0.52	0.105	0.09	0.072
constant	R_β	R_k	R_w	TKE Prandtl number		SDR Prandtl number	
value	12	12	6.2	2		2	

3.2 Validation of the drag coefficient

The correct prediction of a single stem drag a key point in the VP's bulk drag prediction. Considering the same geometry of each stem and the same dimensionless grid resolution around each stem, one representative subregion, a single stem along with its mesh, was extracted from the original whole mesh. Uniform velocity inlet boundary condition and free stream outlet boundary condition are used on this subregion mesh, while having a Reynolds number (Re_d=1000) of stem as in the original whole mesh. Due to the subcritical flow pattern, the dimensionless mesh scale, $\Delta r / d$, was selected as 1/15 and 1/30 for the mesh independent study. The simulation predictions of drag coefficient (C_d) agree well with some existing experimental and numerical results as shown in Table 4. There was little difference in C_d of different mesh resolution, meeting the mesh independence requirement. Thus, for the present VP flow study, the mesh scale in the near cylinder region the dimensionless mesh space, $\Delta r / d$ =1/15. One should also note that Braza et al. (1986) predicted C_d well with a similar dimensionless mesh space, $\Delta r / d = \pi / 50$.

The detailed information, including the definition of C_d, C_l, refined meshes, and time history of C_d, C_l, for this validation are given in the supplementary materials.

Table 4 Comparisons of the time-averaged drag coefficients of circular cylinder with Re_d=1000

Method	Researchers	C_d	$\Delta r/d$
	Braza et al. (1986)	1.15	$\pi / 50$
Numerical	This study	1.24	1/15
	This study	1.25	1/30
Experimental	Roshko. (1961)	1.2	-
	Zdravkovich. (1997)	1.24	-

4. Results and discussions

The results of the flow pattern, channel bed shear stress and the drag coefficients were obtained by 3D URANS RSM VOF method from the twelve designed cases.

4.1 Flow diagnosis

The hydrodynamics of partially vegetated curved channel flow is generated by the combined effects of helical flow (cross-section secondary flow) and mixing layer (shear layer) flow in the edge of VP. This flow diagnosis focuses on investigating the streamwise velocity distribution and secondary flow in two critical cross-sections (the 130-degree cross-section in the vicinity upstream of the VP and the 180-degree cross-section in the near downstream of the VP), which are displayed in Fig.2(a). Next, the dimensionless transverse profiles of velocity, Reynolds stress, and eddy fluctuation frequencies are also investigated in a mixing layer (a sample line AB). More detailed information of the sample line AB is presented in section 4.1.3.

4.1.1 The flow pattern in the 130-degree cross-section

Owing to the subcritical flow condition in the present channel flow (Fr = 0.168 < 1.0) the information of flow in the VP can be transferred to the upstream 130-degree cross-section. The VP has a retardant effect on secondary flow development in 130-degree cross-section, as comparing the streamlines presented in Figs.6(a)(b)(c). The different structures of the outer-bank cell(s) mainly result from the redistribution of the Reynolds stress components (Kashyap et al., 2012, Blanckaert and De Vriend, 2004) and the obstruction of vegetation. Comparing in the cases No.1, No.5 and No.9, the existence of VP makes the main circulation cell of the secondary flow move towards the outer bank, and the greater SVF of VP, the greater the distance the core of that cell moves. Also, the three outer-bank cells are significantly weakened or even disappear by the diverging flow generated in the front of vegetation region.

The *CR* also affects the secondary flow's structure reconfiguration. The *CR* factor is isolated by comparing results in Figs.6(b)(d)(e)(f). The variation of the main circulation cells and the outer-bank cells are discussed in two parts as follows.

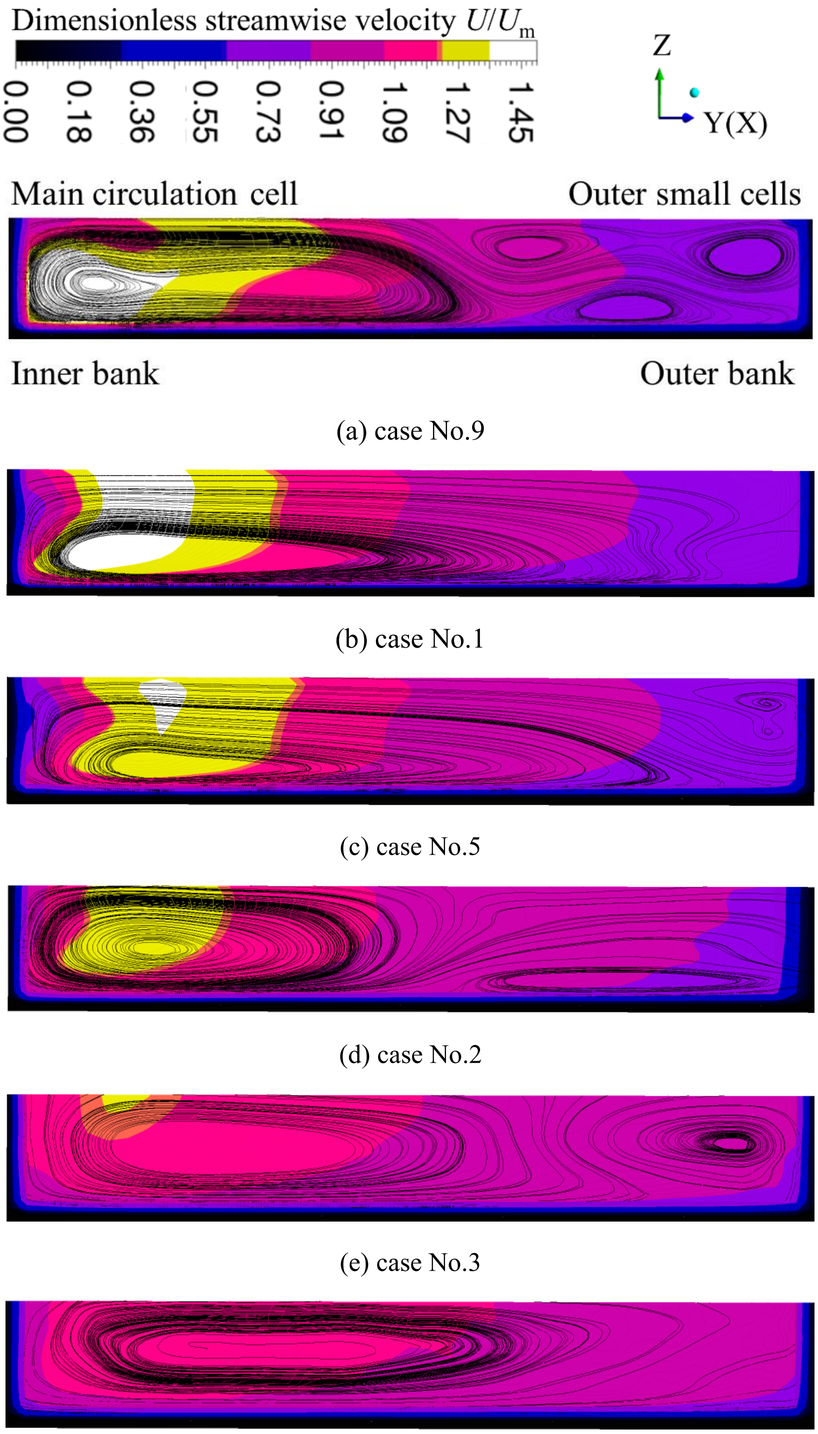

(a) case No.9

(b) case No.1

(c) case No.5

(d) case No.2

(e) case No.3

(f) case No.4

Fig.6 The contours of dimensionless streamwise velocity U/U_m distribution and 2D streamlines in 130-degree cross-section with different *CR*s and SVFs. As denoted in Fig.6(a), the left-hand side is the inner bank while the right-hand side is the outer bank for all contours (a)~(f). The location of 130-degree cross-section as illustrated in Fig.2(a). Fig.6(a) is the dimensionless streamwise velocity contour plot of the non-vegetated case No.9 in Table 2 with a *CR*=0.5. Likewise, the detailed information for other cases please refer to Table 2.

The location of the main circulation cell is closely related to *CR* condition. Simulation results show that the increase of *CR* makes that main cell location move significantly to the outer bank under the same SVF condition. This finding is consistent with a conclusion made by a previous parametrical study of 135-degree flat bends (Kashyap et al., 2012). The outward motion of the core of the main circulation cell is mainly because of the local difference between the outward centrifugal force and inward pressure gradient. With the increase of *CR*, both the outward centrifugal force and inward pressure gradient decrease, but the inward pressure gradient drops faster than the outward centrifugal force.

The formation of the outer-bank cell can be explained by the anisotropic effects of turbulence and the driving forces from the main circulation cell. As the *CR* increases, the decrease of centrifugal force plays a role in the relocation of the outer-bank cell. Comparisons are made between the present simulation case No.3 and the simulation results conducted by Huai et al., (2012) because of similar U-bend geometry features. In their case, as shown in Fig.4, their geometry is a U-bend channel (*CR*=1.5 and SVF=1.13%) covered with a continuous vegetation region close to the inner bend rather than the single VP at the bend exit. Thus, the main difference is that the diverging flow bypassing the leading edge of VP in the present case No.3, while there is no diverging flow at the 135-degree cross-section in Huai's case. However, this diverging flow seems to have little influence on the secondary flow structure in the upstream cross-section of VP. In both cases, the main circulation cell occupies the main non-vegetated channel region, despite that the presence of a continuous vegetation stripe squeezes the main circulation cell move outwards. Nevertheless, both the present simulation case No.3 and Huai's case capture the outer-bank cell close to the intersection between the free surface and outer bank nearly in the same location in the 135-degree cross-section.

However, when we examine the flow pattern in the 180-degree cross-section, we notice the significant difference of the outer-bank cell in both cases. In Huai's case, the outer-bank cell continues from the 135-degree cross-section to the 180-degree cross-section and stays close to the free surface of the flow. By contrast, in the present case No.3, the outer-bank cell disappears in 180-degree and even the main circulation cell disappears, as shown in Fig.7(e), owing to the diverging flow that bypasses the VP and strongly shifts the streamwise velocity distribution. In addition, the small outer-bank cells close to the free surface usually reduce the streamwise velocity gradient and protect the erosion of the outer bank (Kashyap et al.,2012). Thus, the erosion of the outer bank may be promoted if the VP grows in the current location.

4.1.2 The flow pattern in the 180-degree cross-section

By comparing Figs.7(a)(b)(c), the presence of vegetation diminishes the main circulation cells and deflects the main flow outwards at the 180-degree cross-section. Water flux close to the inner bank is substantially reduced due to the blockage of the VP. Moreover, for a VP with a higher SVF shows a stronger capability to shift the maximum streamwise velocity point outwards.

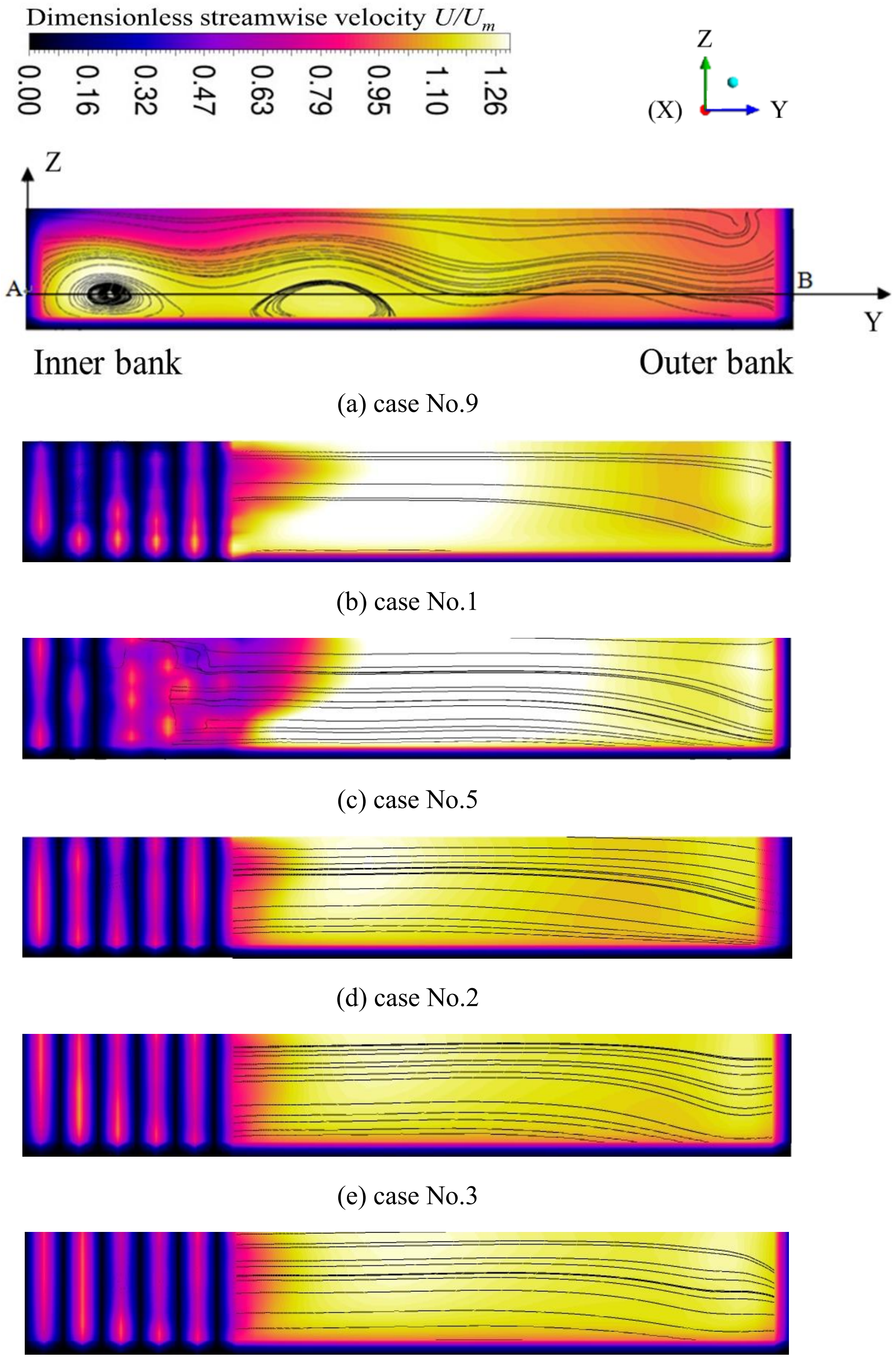

(a) case No.9

(b) case No.1

(c) case No.5

(d) case No.2

(e) case No.3

(f) case No.4

Fig.7 The contours of dimensionless streamwise velocity U/U_m distribution and 2D streamlines in 180-degree cross-section with different *CR*s and SVFs. The location of 180-degree cross-section is illustrated in Fig.2(a). As denoted in Fig.7(a), the left-hand side is the inner bank while the right-hand side is the outer bank for all contours (a)~(f). In Fig.7(a) a sample line AB (A side is inner bank; B is outer bank) is selected in the 180-degree cross-section to quantitatively study key physical variables. Fig.7(a) is the dimensionless streamwise velocity contour plot of the non-vegetated case No.9 in Table 2 with a *CR* 0.5. Likewise, the detailed information for other cases please refer to Table 2.

4.1.3 The mixing layer flow

Mixing layer flow is a key feature in the lateral edge of the VP. To quantify the profiles of velocity, Reynolds stress and dominant frequency of this mixing layer flow, a horizontal line AB is sampled in the 180-degree cross-section (Z=0.06B, B is the width of the bending channel, 1m) in Fig.7(a). This sample line crosses through the main circulation cell centre where the secondary flow velocity components vary fast along this line. In vegetated cases, the mixing layer is ubiquitous in the tips of submerged vegetation or the lateral edges of patches. Ghisalberti and Nepf (2002) used the mixing layer theory to explain the flow profiles over a submerged canopy. The inflection in the velocity profile is proportional to the height of the canopy in their case. Their study shows that the mixing layer in the vertical direction matches well the theoretical prediction. Following this finding, Huai et al. (2019) found that for a straight channel partially covered by emergent vegetation, the streamwise velocity inflection layer in the interface between the vegetated region and non-vegetated region also obeys the mixing layer theory in a horizontal direction. Nevertheless, previous studies focus on the rigid submerged or emergent vegetation in a straight channel without the bending effects and the variation of SVF. Therefore, in the present bending channel, a quasi-horizontal mixing layer develops over the edge of the VP. The streamwise velocity profile along the spanwise is re-distributed by the secondary flow, which is also sensitive to the SVF but we have little understanding to what degree of *CR* and SVF influence the effectiveness of planar mixing layer theory in bending channel cases. As a result, Fig.8 displays the normalised velocity profiles in all present *CR* and SVF conditions. Those profiles are also compared to the hyperbolic tangent law of the mixing layers which is expressed by (3).

$$\frac{U-\bar{U}}{\Delta U}=\frac{1}{2}\tanh\left(\frac{Y-\bar{Y}}{2\theta}\right), \tag{3}$$

$$\theta=\int_{-\infty}^{+\infty}\left[\frac{1}{4}-\left(\frac{U-\bar{U}}{\Delta U}\right)^2\right]dY. \tag{4}$$

the momentum thickness θ is defined by (4) (Ghisalberti and Nepf, 2002). U is the streamwise velocity, $\bar{U}$ is mean streamwise velocity including the vegetated region and non-vegetated region. The velocity difference, ΔU, between the cross-sectional averaged streamwise velocity in vegetation region, $\overline{U_1}$, and that of non-vegetated region, $\overline{U_2}$, is $\Delta U=\overline{U_2}-\overline{U_1}$. Y is the spanwise coordinates. $\bar{Y}$ is defined as a location where $U=\bar{U}$.

As shown in Fig.8, it is highlighted that the simulation results of the velocity profiles along the AB in the region of the mixing layer are in agreement with the theoretical predictions, i.e. hyperbolic tangent law of the mixing layers, whatever the variation of the bend *CR* and SVF are in the present range of those variables. These results indicate that the stronger secondary flow circulation, resulting from the tighter bend, strengthens the streamwise velocity difference, ΔU, but weakly alters the normalised mixing layer velocity profiles.

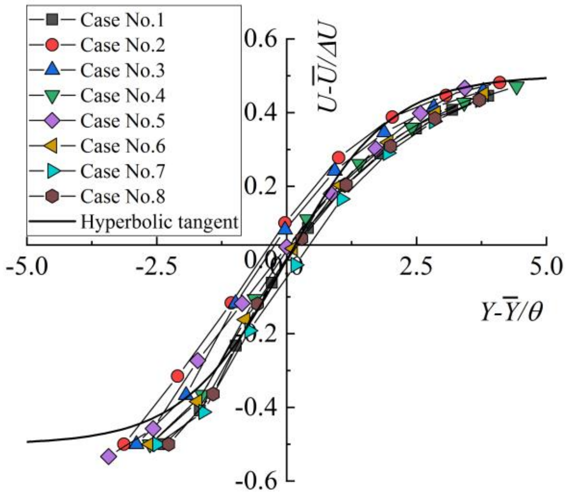

Fig.8 the normalised mixing layer velocity profiles along line AB in the region of (0.25<*Y/B*<0.45). In this region the mixing layer happens. The plots present the normalised mixing layer velocity profiles under all vegetated cases. The cases parameters are given in Table 2.

The vertical velocity component (*W*) profiles along AB present the secondary flow directly. Fig.9 makes comparisons for *W* and shows that the existence of VP strongly diminishes the secondary cells in the near downstream patch region (0<*Y/B*<0.25). An interesting observation for all vegetated cases is that the upward vertical velocity mostly happens in the patch region downstream (0<*Y/B*<0.25), by contrast the downward vertical flow locates in non-vegetated region (0.6<*Y/B*<1.0). This is because the vegetation highly improves the roughness of the channel and shifts the flow system to a new equilibrium under the drag effects from the vegetation, the spanwise pressure gradient and the centrifugal force. This finding theoretically supports the fine sediment resuspension event observed in sparse meadows (Van Katwijk et al., 2010, Luhar et al, 2008). Luhar believed that the SVF threshold indicator is around 10%, if the drag coefficient is assumed to be 1.0. For the sparse VP (SVF<10%), the upward flow velocity component *W* enhances the resuspension of particles near the channel bed. All the present cases the SVF are lower than that threshold, which leads to the upward velocity in the downstream of VP.

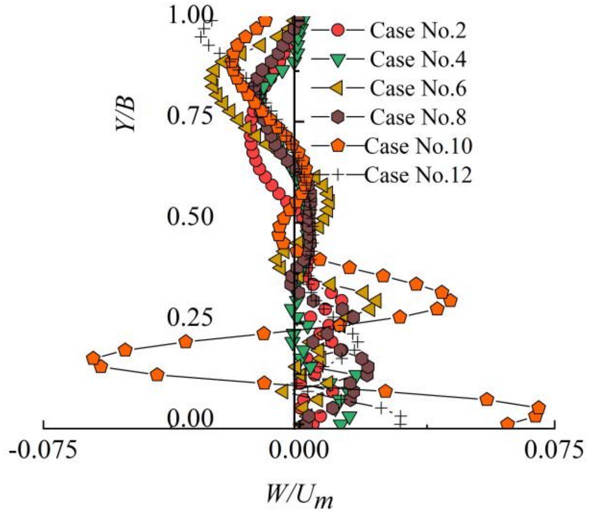

Fig.9 Normalised vertical velocity in Z direction, W/U_m, profile along sample line AB. The location of line AB is displayed in Fig.7(a). $0<Y/B<0.25$ is the downstream of patch region, $0.25<Y/B<1$ is non-vegetated region. The cases parameters are given in Table 2.

The Reynolds stress component $-\overline{u'v'}$ demonstrates the shear strength along a sample line (u' and v' are streamwise and spanwise velocity fluctuations, respectively). The peaks, located in Y/B=0, 1.0, are because of the boundary layer of the channel bank. However, the deflection in Y/B=0.25 is due to the mixing layer induced by the VP. Furthermore, the spanwise momentum exchange in spanwise induced by the turbulent motions can be described by the magnitude of this Reynolds stress component (Tennekes and Lumley, 1972). Also, the $-\overline{u'v'}$ growth in Y/B=0.25 implies that the vortices enhance the spanwise transport of momentum. In straight channel cases, this kind of mixing layer Reynolds stress component increase is also noticed (Huai et al. 2015). Fig.10 displays $-\overline{u'v'}$ profiles alone sample the line AB (in Fig.7(a)), which indicates the shear strength of the flow in a horizontal plane.

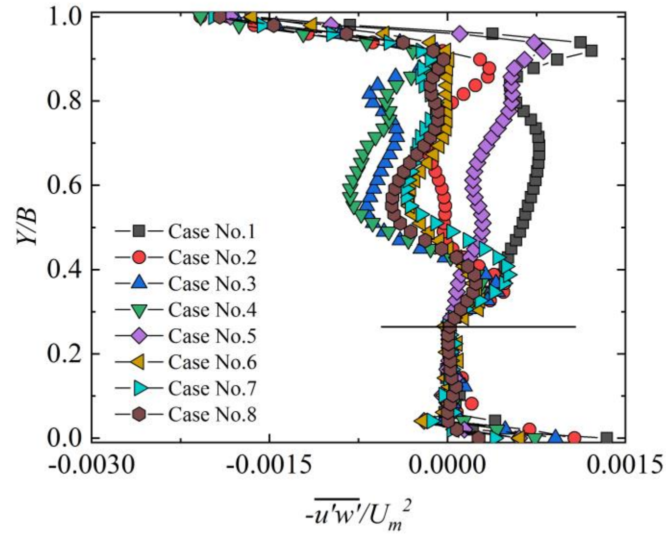

Fig.10 Reynolds stress profiles along sample line AB. *u'* and *v'* are streamwise and spanwise velocity fluctuations, respectively. The cases parameters are given in Table 2.

The dimensionless dominant eddy frequencies (St_e) are presented along the line AB in Figs.11(a)(b). The definition of St_e is shown in equation (5)

$$St_e = \frac{f_e \cdot l}{U_m}. \tag{5}$$

Where f_e is the local dominant eddy frequency which is estimated by extracting the dominant cyclic fluctuation of velocity history in points along line AB. l is the length scale of VP, L is chosen for l in current case, U_m is average inlet velocity. Figs.11(a)(b) indicate that the effects of VP highly increase the dominant eddy frequencies in the downstream of the patch region (0<Y/B<0.25), as compared to the non-vegetated region (0.25<Y/B<1.0). This is because the VP shifts the large-scale eddies of channel width length scale into that of the vegetation stems' scale by generating vortices shedding and the vortices interactions. According to the basic turbulence theory the smaller turbulence scales correspond to higher eddy frequencies. The transition region (0.25<Y/B<0.4) in the lateral side of the VP experiences a gradual decrease of the eddy frequency from a vegetated region to a non-vegetated region since the mixing layer length scale is larger than stem diameter scale but is smaller than channel width scale.

Having a deeper look in those frequencies' profiles, we surprisingly discover that these dimensionless eddy frequencies profiles (St_e) are strongly altered by the choice of normalised length scale. When the frequencies are normalised using their stem diameters d=6mm (SVF=1.13%) and 12.45mm (SVF=4.86%), in Fig.11(a), the data gather into three profile groups marked by different SVF conditions. However, in comparison, those frequency data of vegetated cases collapse nearly into one profile, in Fig.11(b), when these frequencies are normalised by the spanwise VP length scale (L=0.25m). This reveals that the length scale of VP also plays an important role in determining the downstream eddy frequencies of a VP. What also stands out is that the dimensionless frequency profiles experience little change while the *CR* varies. This is probably because the dimensionless frequency is dominated by the streamwise flow velocity which is not as sensitive as the secondary flow, when affected by the *CR*. Thereby, for a specific SVF (1.13% or 4.86%) the eddy frequency profiles of different *CRs* nearly collapse into one plot.

By comparing the dimensionless eddy frequency normalised by stem diameters in Fig.11(a) to that of a single stem (cylinder) in literature, we conclude that the eddy frequency of a stem in a patch is much higher than a single stem. The vortex shedding frequency, St_d, for a single stem (cylinder) is nearly 0.2 where Re_d=1000~100000. In contrast, the eddy frequencies (St_d) for a stem in the present patch are around 0.6 and 1.4 for d=6mm (SVF=1.13%) and 12.45mm (SVF=4.86%), respectively, whose St_d are much over than that of a single cylinder. The main reason is that the vortex shedding process of a stem in the VP is enhanced by interactions of neighbouring vortices developed from upstream stems and lateral side ones. The interaction mechanisms can be categorized into two types: The streamwise vortex interference and spanwise interference. For the streamwise interference category, the vortices generated by the upstream cylinders impinge on the downstream cylinders and merge to the vortices shedding from the downstream, resulting in "amalgamation process", as shown in Fig.23 in the supplementary materials. For the spanwise side-by-side vortices shedding processes, complex vortices interact in the combined wake of cylinders in present vegetation stems' configuration and Reynolds number (1000~3000) (Sumner, 2010). All of these wake interactions considerably generate smaller scale eddies and increase eddies' frequencies.

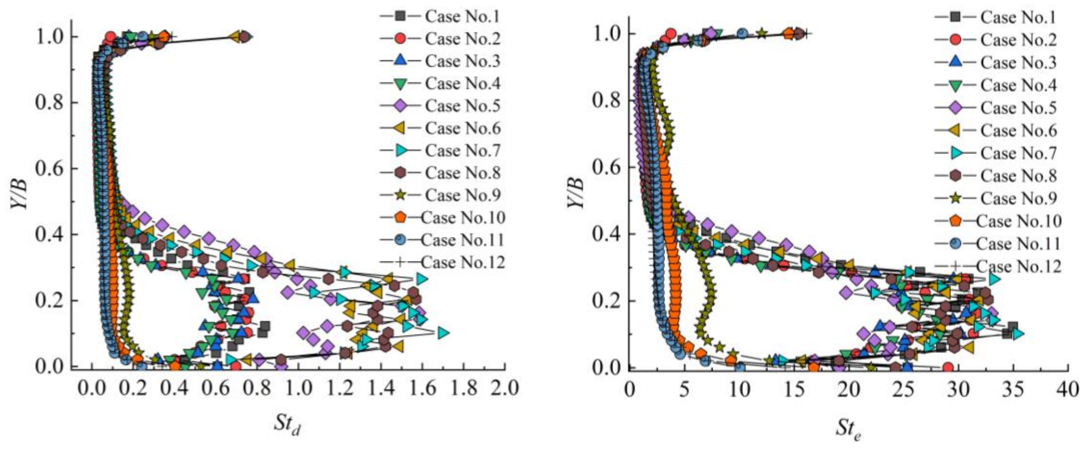

(a) (b)

Fig.11 Eddy frequency profiles along the sample line AB: (a) frequencies normalised by the vegetation stem diameter d=6mm and 12.45mm corresponding to SVF=1.13% and SVF=4.86% respectively. (b) frequencies normalised by the VP width scale (L=0.25m). The mean inlet velocity U_m=0.2 m/s is used as the normalise velocity in both (a) (b). The cases parameters are given in Table 2.

4.2 Bed shear stress

The dimensionless of bed shear stress i.e. friction coefficient of channel bed, C_f , is defined in expression (6):

$$C_f = \tau / \rho U_m^2. \tag{6}$$

Where τ is bed shear stress, ρ is the density of water, U_m is the inlet averaged velocity.

4.2.1 Qualitative study of the bed shear stress in the whole U-bend region

The bed shear stress of the area close to the inner bank is significantly larger than that of the outer bank owing to the uneven distribution of the mainstream velocity. This finding is consistent with that of Kashyap et al. (2012). However, in the present findings, we highlight that the stress discrepancies between the inner area and the outer area experience a significantly increasing trend as the *CR* decreases, as shown in Fig.12. This is because the main stream's relocation controlled by the variation of *CR*, and the larger vertical velocity gradient is located at the bottom of those mainstreams. This process can also be viewed in details in the zoom-in views of contours in Fig.14.

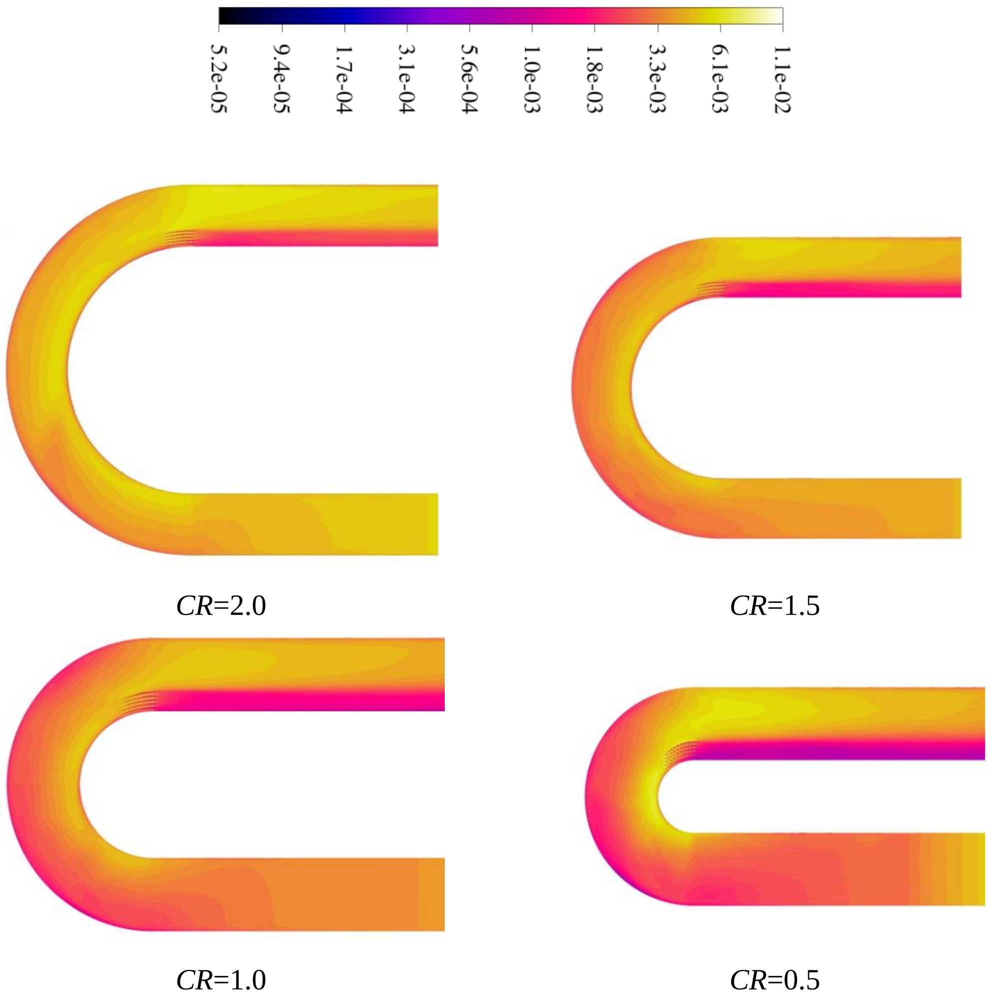

Fig.12 The contours of bed shear stress coefficient, C_f, under the variation of *CR* from 0.5 to 2.0 with SVF=1.13% corresponding to case No.1 to case No.4.

4.2.2 Quantitative study of the bed shear stress in the whole U-bend region

To quantitatively study the relationship between the *CR* and bed shear stress, Figs.13(a)(b) present the location and value of maximum shear stress points along these channel bends, linking the sample points plots the thalweg of the channel, where the erosion event firstly occurs. Some researchers proposed good discussions on the relationship of hydraulics, bed shear stress and thalweg in channel bends by using the 2D models (Bywater-Reyes et al., 2018, Crosato and Saleh, 2011, Wu et al., 2005), but discussions on the variations of the thalweg of these partially vegetated river bends under different *CR* conditions are very limited. Here, we provide a discussion on this topic. Note that the relative location of thalweg displayed in Fig.13(a), where *Y/B*=0, 1.0 correspond to the inner bank and outer bank, respectively.

Fig.13(a) clearly shows that the relative location of the maximum bed friction coefficient (C_f) lines plotted by linking the maximum C_f of each cross-section under different *CR* conditions. These lines gradually move away from the inner bank towards the central axis of the channel bed with the increase of *CR,* especially in the bending region (0, 120). The main reason is less bending, thus less secondary flow and more uniformity in the spanwise velocity profile. This conclusion is also consistent with the extreme case where the relative position of the maximum section shear stress line is in the middle of channel bed (*Y*/*B*=0.5) in a straight channel (*CR* approaches to infinite).

Fig.13(b) shows the maximum value of the shear stress in each cross-section, corresponding to locations illustrated by Fig.13(a). In all areas including non-vegetated and vegetated areas, the magnitude of the maximum section shear stress increases with the drops of *CR*.

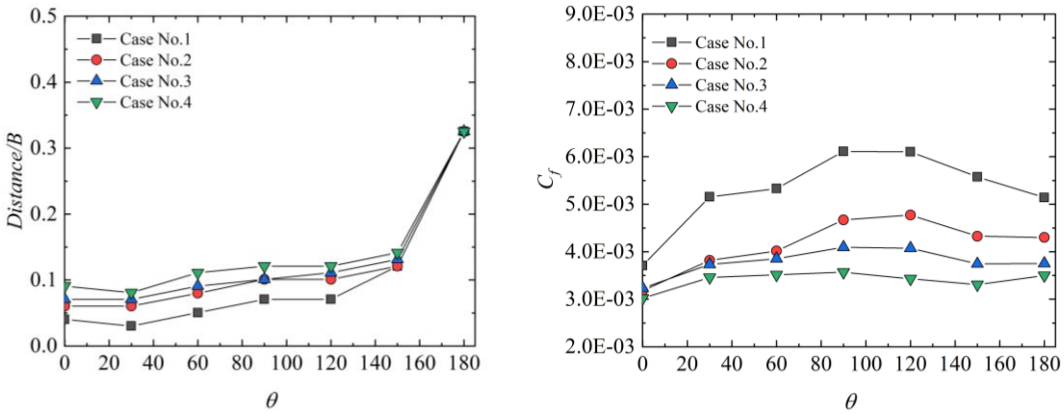

(a) (b)

Fig.13(a) Normalised location of maximum bed shear stress lines by linking maximum bed shear stress points in each cross-section (0,30,60...,180). (b) The magnitude of maximum bed shear stress points in those cross-sections. The normalised position (*Distance/B*) is defined as the ratio between the distance of the maximum bed shear stress point to the inner bank to the width of the channel (B). The maximum bed shear stress on the cross-sections of the curved bends are collected every 30 degrees from 0-degree to 180-degree along bending channels corresponding to the entrance and exit of the half-circle bend. C_f denotes the normalised bed shear stress. The cases parameters are given in Table 2.

4.2.3 Qualitative study of the bed shear stress in the vegetated region

Having a zoom-in observation in the VP region in Fig.14, there is a notable increase of the bed shear stress at the patch's leading edge, because of the existence of the plants group. The water flow bypasses the sides of the vegetation stems, where the water flow is squeezed and speeds up. Thereby, the stems on the inner side of the curved channel initially increase the possibility of scouring at the beginning of vegetated region, rather than protecting the channel bed. The stems near the central line of the channel also suffer a strong erosion. This patch side edge erosion accords with the observation of Rominger et al. (2010). What we stress here is that the tighter bend suffers a higher local bed shear stress in the leading edge and lateral edge.

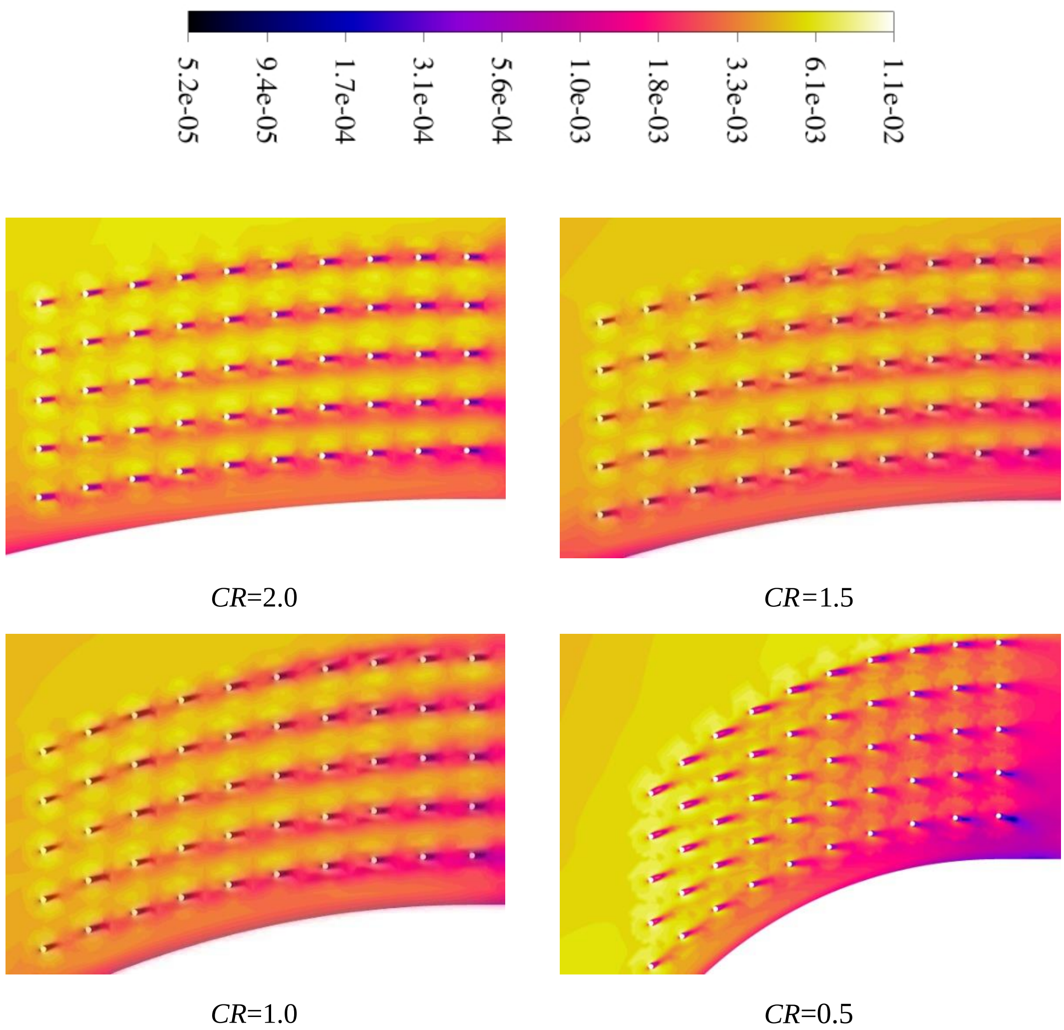

Fig.14 The bed shear stress coefficient, C_f, distribution. These contours are the zoom-in views of vegetated areas in Fig.12, corresponding to case No.1~4.

4.2.4 Quantitative study of the bed shear stress in the vegetated region

To quantify the blockage effects of VP on the local bed shear stress under the variation of *CR*, the spanwise bed shear stress profiles in the near downstream of the VP (the intersection of 180-degree cross-section and channel bed), is plotted in Fig.15. This plot indicates that the maximum bed shear stress (Y/B=0.35) at non-vegetated region drops with the rising of the *CR*. This indicates that the strongest shear stress happens at the tightest bend (*CR*=0.5) in which case the strongest centrifugal force effectively redistributes the main flow.

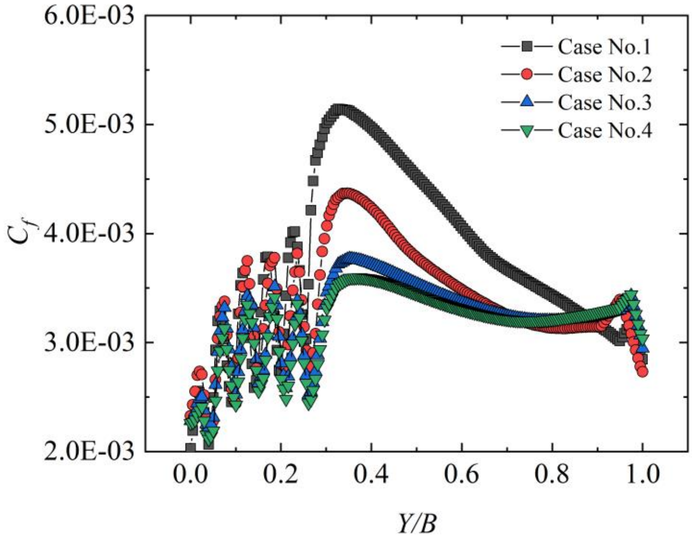

Fig.15 The bed shear stress coefficient, C_f, distributes on the intersection line between 180-degree cross-section and channel bed under different *CR* conditions. The cases parameters are given in Table 2.

4.3 Dynamic forces on quasi-rectangular VP in curved channel

Most previous studies focused on the drag of VP in a straight open channel, however, the drag characteristics of VP in a curved channel have not been recorded in literature to the authors' knowledge. Especially, the relationship between the drag coefficients of VP and the *CR* of a channel. The findings of drag coefficients in a bending channel are presented in Fig.16.

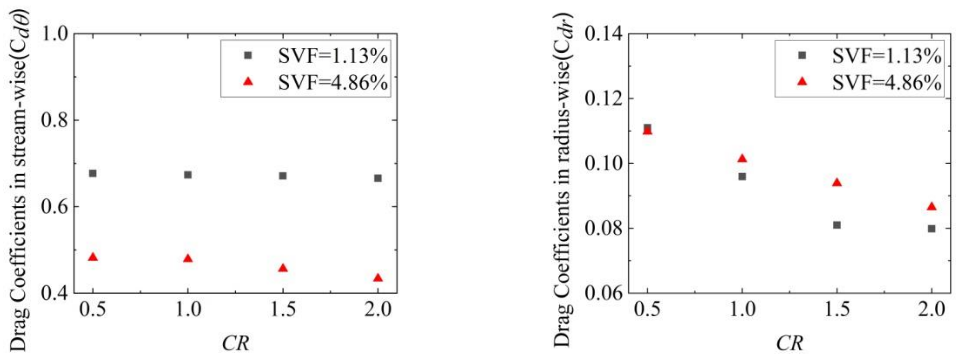

(a) (b)

Fig.16. The relationship between the *CR* and drag coefficients in streamwise, $C_{d\theta}$, and spanwise (radius-wise), C_{dr}.

Those time-averaged drag forces are normalised by $\frac{1}{2}AN\rho U_m^2$, as is shown in Eqs. (7) and (8).

$$C_{dr} = \frac{F_r}{\frac{1}{2}AN\rho U_m^2}, \tag{7}$$

$$C_{d\theta} = \frac{F_\theta}{\frac{1}{2}AN\rho U_m^2}, \tag{8}$$

where F_θ, F_r, A, N, ρ, U_m are the streamwise VP drag force, radius-wise VP drag force, projection area of a single stem, total number of stems in a patch, density of water, and inlet average velocity. Those time-averaged drag coefficients exerted on these patches are decomposed into a streamwise component ($C_{d\theta}$) and radius wise (spanwise) component (C_{dr}). They are displayed in Figs.16(a)(b) highlighting that there is a slight fall trend of $C_{d\theta}$ as the *CR* increases in the eight cases, but an obvious decrease of C_{dr}. The redistribution of the main flow velocity profile controlled by *CR* leads to this fall trend for $C_{d\theta}$. Under the decrease of the secondary flow circulation results in a significant drop of C_{dr}. It is interesting to find that the C_{dr} is clearly more sensitive than $C_{d\theta}$ under the variation of *CR*, and also the ratio $C_{dr}/C_{d\theta}$ is in the range of 5%~15%, therefore, the spanwise pushing effect from the VP to flow may need to be taken into consideration in practical engineering cases.

4.3.1 Local stems' drag rising phenomenon in a VP

In order to study the drag distribution in more detail, the time-averaged drag coefficients on each row in streamwise ($C_{d\theta i}$ (i=1~10)) are recorded. The $C_{d\theta i}$ (i=1 to 10) are presented in Fig.17. Set the leading row of VP as Row No.1 and the very downstream as Row No.10.

As expected, after the flow bleeds into VP, the flow velocity decrease gradually leading to the decrease of $C_{d\theta i}$ in an overall view, as illustrated by Fig.17. However, it is surprising to notice that $C_{d\theta i}$ experiences a locally rising trend in Rows No.3~5 with SVF=4.86%. This is owing to the skewness of stems' location in the bending area, a kind of staggered distribution stems formed in this region, as shown in Fig.14. The authors discover the dominant reasons for this rising trend includes the staggered distribution of stems and the proper SVF. These stem rows are nearly situated in the trajectory of vortices shedding from the upper vegetation rows. Periodical flow contacts from the vortices transported from the upstream can lead to a higher drag as well as stronger flow fluctuations than that of the upstream row of stems because of the collision between the upstream vortices (higher momentum carrier) to downstream stems.

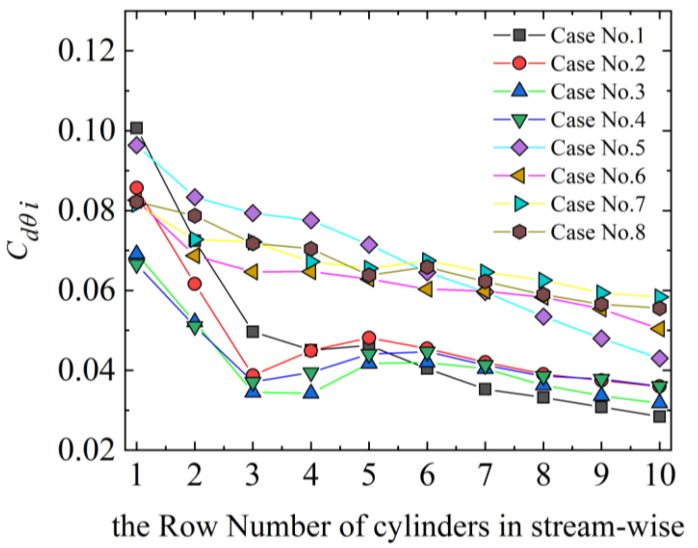

Fig.17 The time-averaged streamwise force coefficients of each row of stems, $C_{d\theta i}$, along the streamwise direction. The row of stems are numbered from Row No.1 to Row No.10 from the upstream location to downstream location in VP. The cases parameters are given in Table 2.

Interestingly, this local stems' drag rising phenomenon, in a VP, was also displayed in (Chang and Constantinescu, 2015, Fig.16(c), Fig.18) although not explicitly discussed. In their configuration, a circular VP with a staggered distribution was located in a straight open channel flow with a similar SVF (5%). Thus our study concludes this finding for bending channel up to CR=2.0.

In this SVF (4.86%~5%) is neither too high to prevent the flow penetrating into the patch but not too low to neglect the interaction between streamwise vortices. In comparison with SVF=4.86% in the present study, the VP with SVF=1.13% does not present this kind of drag coefficients' local rising in the VP, due to the low SVF condition. Likewise, the staggered distributed circular VPs in the straight channel (Chang and Constantinescu, 2015) also do not have such local drag rising when their SVF is 0.2, 0.1, 0.0023, except for the cases with SVF=0.05. These findings demonstrate that proper SVF (around 5%) is also a key factor for this phenomenon. Moreover, all of the observations whether in a bending or a straight channel also imply that the CR is not the dominant factor for this physical phenomenon.

Furthermore, there is a close relationship between the CR and the average drag gradient. Here, we define the drag gradient as $(C_{d\theta\ 1}- C_{d\theta\ 10})/Ls$, where the Ls is the streamwise length between stems Row No.1 and stems Row No.10. In both SVF conditions, the drags' gradients reach the highest when the CR is lowest (CR=0.5). The drag gradients of the stem rows gradually fall when the CR grows. The drag coefficient gradient can be a good indicator to reveal the "slowing down" effects exerted by stems to the flow in the vegetated region. Thereby, Fig.18 demonstrates that this velocity reduction effects altered by the *CR* is sensitive to the SVF factor. For a higher SVF (4.86%), this reduction effect is more significant than that for lower SVF (1.13%) cases.

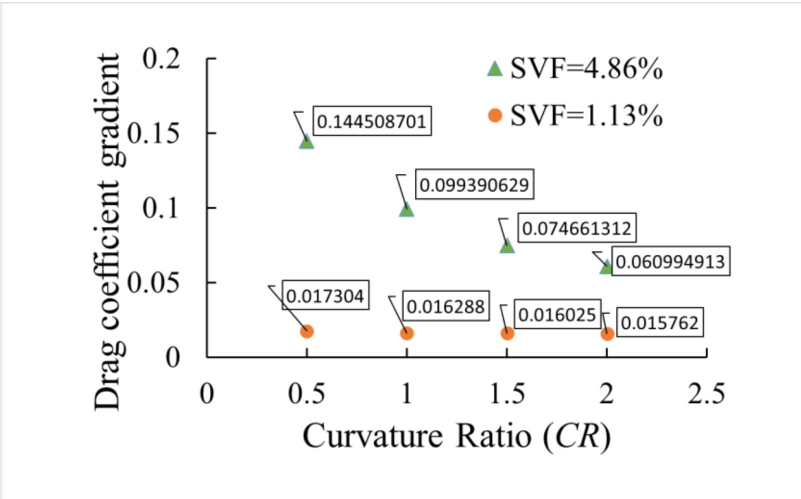

Fig.18 The relationship between the *CR* and streamwise drag coefficient gradients. The definition of the drag gradient is ($C_{d\theta\ 1}$- $C_{d\theta\ 10}$)/Ls, where the Ls is the streamwise length between stems Row No.1 and stems Row No.10, illustrated in Fig.2(b).

4.3.2 The relationship between the St_p and SVF

For a deeper understanding of the streamwise bulk drag coefficient ($C_{d\theta}$) in the frequency space, the time series of $C_{d\theta}$ are transferred into the frequency domain using Fast Fourier Transform (FFT). In each case, there is a dominant frequency peak revealing the main vortices' shedding frequencies as well as other periodical flow events. This dominant frequency is normalised by L/U, where L is the spanwise scale of VP. The dominant dimensionless frequency (St_p) of a VP's vortices shedding describes the main shedding cycles of the main flow structures after flow bleeding or bypassing the VP. The spectra analysis results are compared in the same *CR* condition and are presented in Fig.19.

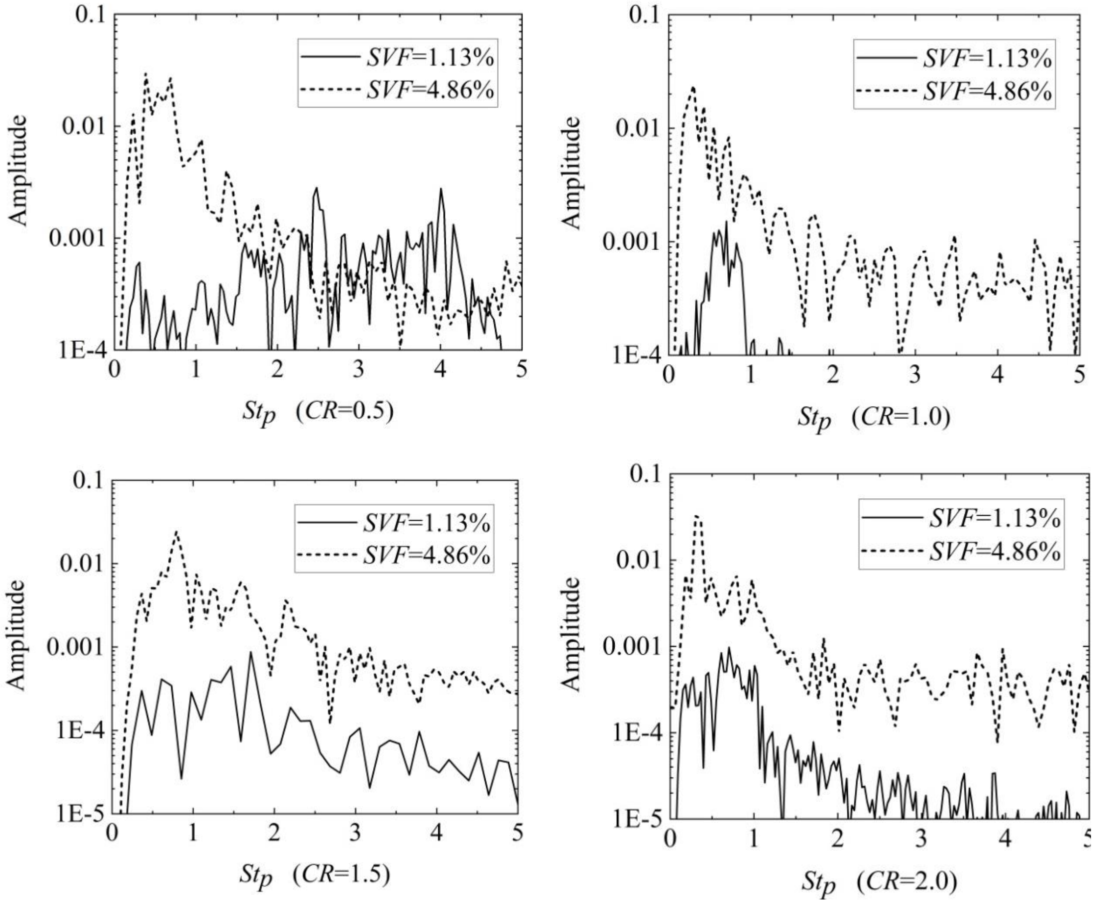

Fig.19 Comparisons of amplitude spectrum of the VP drag in each *CR* condition with different SVFs.

Zhang et al. (2019) found that the dimensionless peak frequency of their case 1, circle VP with SVF=0.034 in straight channel, is smaller than their case 2, circle VP with SVF=0.0104 in straight channel, and concluded that the dimensionless dominant frequency of force coefficient decreased along with higher SVF. This conclusion from Zhang et al. (2019) is constructive, but we are not sure whether this conclusion is valid for all the range of SVF from 0 to 1, because there are only two test cases in their study and no more data support their conclusion. Thereby, we tried to explore the effective range of SVF where St_p can be inversely proportional to SVF.

More data were collected from literature (Zhang et al., 2019, Chang and Constantinescu, 2015, Nicolle and Eames, 2011) and plotted together with the present results in Fig.20. We newly find that the conclusion proposed by Zhang et al., (2019) is merely valid for 0<SVF<10.4%. By contrast, in the subrange for 10.4%<SVF<20%, the dimensionless frequency may increase with the rising of the SVF. Therefore, we make a new conclusion that only in the range 0<SVF<10.4%, the increase of SVF results in the decrease of dimensionless frequency, however, in the range 10.4%<SVF<20% this trend is inversed. However, in reality, the range, 0<SVF<10.4%, covers most SVF of marsh grass and sea grass species (Nepf, H.M., 2012), therefore in the following section 4.3.3, a quantitative discussion on the relationship between the dimensionless dominant frequency and SVF is discussed in that range.

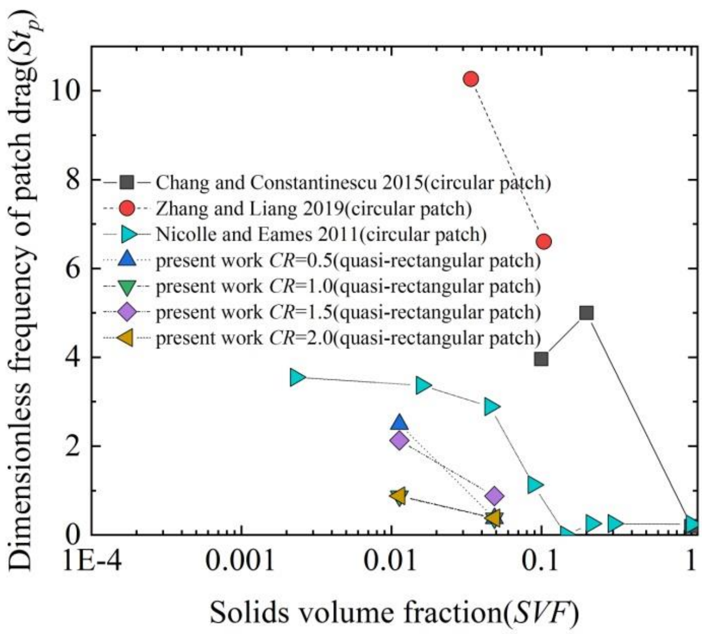

Fig.20 A collection of the relationship between SVF and dimensionless frequency of VP vortices shedding (St_p) in different patch shapes and flow conditions. The points linked by lines are of a similar geometry with the same patch shape factor and same stems distribution factor.

4.3.3 A new VP dimensionless number, $St_p \frac{\sqrt{\mathrm{SVF}}}{\sqrt{N}}$

As mentioned before, Strouhal number (*St*) is a dimensionless frequency number describing oscillating mechanisms. For a solid single cylinder, the St_d is defined as

$$St_d = \frac{f\,d}{U} \tag{9}$$

where f, d, U are the frequency of vortex shedding, diameter of cylinder, flow velocity. For a single cylinder, the Strouhal-Reynolds (St_d-Re_d) number relationship has been studied extensively. St_d varies between 0.18 and 0.22 when Re_d is in the range from 500 to 10000 (Jiang and Cheng, 2017, Blevins, 1990). As analogous to the definition of single cylinder case, a dimensionless frequency for a VP is defined as follows:

$$St_p = \frac{f_p L}{U}. \tag{10}$$

Where f_p, L, U are the frequency of vortex shedding of VP, spanwise length scale of VP and flow velocity, respectively. By contrast, as compared to a solid single cylinder case, a patch dimensionless frequency, St_p, is not only determined by the VP Reynolds number, Re_p, but also influenced by the SVF of VP, the number of stems in this patch, N, the stems distribution and the general shape of this VP, which can be expressed in Eq.(11).

$$St_p \sim f\,(Re_p, \mathrm{SVF}, N, \mathit{stems\ distribution\ factor}, \mathit{patch\ shape\ factor}). \tag{11}$$

It is highly interesting that a newly proposed dimensionless number, $St_p \frac{\sqrt{\mathrm{SVF}}}{\sqrt{N}}$, keeps nearly constant for each VP case groups where the stem distribution factor and patch shape factor are the same. In other words, despite the variation of SVF in 0~10.4%, the

$St_p \frac{\sqrt{\mathrm{SVF}}}{\sqrt{N}}$ does not change too much with respect to the variation of St_p in each group. Various cases are presented in table 5.

Table 5 Summary of St_p, SVF, and the VP dimensionless number, $St_p \frac{\sqrt{\mathrm{SVF}}}{\sqrt{N}}$. In each group the stems distribution factor, patch shape factor and Re_p are the same, but the SVF and N are different.

groups	cases	St_p	SVF	N	$St_p \frac{\sqrt{\mathrm{SVF}}}{\sqrt{N}}$	Re_p
1	circular patch flow (Chang and Constantinescu, 2015)	3.958	0.023	10	0.189819	10000
	circular patch flow (Chang and Constantinescu, 2015)	3.958	0.05	21	0.1931306	10000
	circular patch flow (Chang and Constantinescu, 2015)	3.958	0.1	41	0.1954717	10000
2	circular patch flow (Nicolle, and Eames, 2011)	3.55	0.0023	1	0.170252	2100
	circular patch flow (Nicolle, and Eames, 2011)	3.3695	0.0159	7	0.1605887	2100
	circular patch flow (Nicolle, and Eames, 2011)	2.8897	0.0454	20	0.1376784	2100
3	circular patch flow (Zhang et al. 2019)	10.26667	0.034	46	0.2791194	680
	circular patch flow (Zhang et al. 2019)	6.6	0.104	140	0.1798857	680
4	quasi-rectangular *CR*=2	0.7	0.0113	50	0.0105233	50000
	quasi-rectangular *CR*=2	0.3	0.0486	50	0.0093531	50000
5	quasi-rectangular *CR*=1.5	1.7	0.0113	50	0.0255566	50000
	quasi-rectangular *CR*=1.5	0.7	0.0486	50	0.0218238	50000
6	quasi-rectangular *CR*=1.0	0.7	0.0113	50	0.0105233	50000
	quasi-rectangular *CR*=1.0	0.3	0.0486	50	0.0093531	50000
7	quasi-rectangular *CR*=0.5	1.8	0.0113	50	0.0270599	50000
	quasi-rectangular *CR*=0.5	0.6	0.0486	50	0.0187061	50000

Thus, we can interpret the physical meaning of $St_p \frac{\sqrt{\mathrm{SVF}}}{\sqrt{N}}$ as a new patch dimensionless frequency number which excludes the influence of the SVF and N. This newly-constructed dimensionless number affected by remaining factors is expressed in Eq. (12).

$$St_p \frac{\sqrt{\mathrm{SVF}}}{\sqrt{N}} \sim f\,(Re_p, \textit{stems distribution factor}, \textit{patch shape factor})\,. \tag{12}$$

For the influence of Re_p, we notice that in all circular patch cases $St_p \frac{\sqrt{\mathrm{SVF}}}{\sqrt{N}}$ varies between the 0.137 to 0.28 and most of them fluctuate around 0.2, while Re_p is in the range of (680, 10000). This scenario is quite similar to the single cylinder case, where the St_p is around 0.2, while Re_d varies in the range of (500, 10^4). Thereby, we can explain that during the variation of SVF in range of (0, 10.4%), only the mild change of the VP dimensionless number, $St_p \frac{\sqrt{\mathrm{SVF}}}{\sqrt{N}}$, happens. This is partially because in the case of a low SVF, the VP shedding frequency is closely related to the single stem's shedding frequency, and the complicated interactions of the wakes in the VP region may introduce a kind of "noise" information of the dimensionless frequency of the VP.

The patch shape factor also plays an important role in controlling the value of $St_p \frac{\sqrt{\mathrm{SVF}}}{\sqrt{N}}$. As shown in table 5, in all circular patch cases $St_p \frac{\sqrt{\mathrm{SVF}}}{\sqrt{N}}$ varies in the range of 0.137 to 0.28, but in all quasi-rectangular cases its value changes in the range of 0.009 to 0.027. The quasi-rectangular patch dimensionless number is much smaller than that of the circular patch cases, when the Re_p is in the same order O(10^4). Another interesting point that may also support this opinion to some extent, under the same Reynolds number ($10^3 < Re_d < 10^4$), the Strouhal number of a solid single rectangular cylinder (length/width=2), St_d, is around 0.09 (Okajima, 1982), which is much less than that of a solid single circular cylinder (around 0.2). These published results can be understanded that $St_p \frac{\sqrt{\mathrm{SVF}}}{\sqrt{N}}$ is about 0.09 for the rectangular VP (SVF=1, N=1), in contrast, $St_p \frac{\sqrt{\mathrm{SVF}}}{\sqrt{N}}$ equals to 0.2 for a circular VP (SVF=1, N=1). This means that for the solid cases (SVF=1, N=1) the new parameter of the rectangular case is also smaller than that of the circle case. All the discussion above demonstrate that the patch shape factor effectively influences $St_p \frac{\sqrt{\mathrm{SVF}}}{\sqrt{N}}$. Even so, a more systematic study is needed to prove this point of view.

In summary, we draw some findings as follows: for each specific VP (circular or quasi-rectangular), during the decrease of SVF, a patch dimensionless number, $St_p \frac{\sqrt{\mathrm{SVF}}}{\sqrt{N}}$, is proposed to link St_p and SVF. The value of this new dimensionless frequency number for a VP is strongly determined by the patch shape factor and is mildly influenced by the Re_p while already counting for the SVF and N.

5. Conclusions

The hydrodynamics of partially vegetated U-bend channels are studied by URANS numerical method. Main findings on the flow diagnosis, bed shear stress and dynamic forces on VP are summarized as follows.

(1) The existence of a VP in a curved channel flow plays a diverging effect on the streamwise flow, comparing to the non-vegetated case, the location of the main

circulation cell in the upstream is slightly moved towards the outer bank. As *CR* increases, the main circulation cell moves towards outer bank. At the same time, the generation of the outer-bank cells in this cross-section is mildly prevented. For the downstream cross-section, VP diminishes the development of the secondary flow effectively.

(2) The spanwise mixing layer velocity profiles still follow the hyperbolic tangent law of mixing layers under little influence of the variation of *CR* and SVF in the investigated parameters' space.

(3) The effects of a VP highly increase the eddy frequencies in the downside of the patch region ($0<Y/B<0.25$), as compared to the non-vegetated cases. The length scale of the VP also has an important role in the determination of the downstream eddy frequencies of a VP apart from the stems' scale.

(4) VPs have double-side effects on the bed shear stress, increasing the possibility of scouring at the leading part of VP, but decreasing the bed shear stress in the downstream region. Augmentation of the *CR* shifts the location of the thalweg closer to the channel centre and decreases the magnitude of the bed shear stress along the thalweg in the upstream bend region.

(5) For the VP bulk drag coefficient, $C_{d\theta}$ and C_{dr}, experience a fall trend as the *CR* increases in both SVF conditions. For each single stem drag, the local stem's drag growth is studied, and we conclude that the dominant factors for local stems' drag growth are the staggered distribution of stems and the proper SVF (approximately 5%) rather than *CR*.

(6) The dominant dimensionless frequencies (St_p) decrease along with the rising of SVF (SVF<10.4%) for each same geometry. This finding previously proposed by Zhang et al., (2019) was limited to 0<SVF<3.4%. This range was extended to 0<SVF<10.4% in the present study by combining the literature data and the present simulation results. However, the relationship between St_p and SVF interestingly turns into positive correlation in the range of 10.4%<SVF<20%.

(7) A new patch dimensionless frequency number, $St_p \frac{\sqrt{\mathrm{SVF}}}{\sqrt{N}}$, is proposed, which stays nearly constant while the SVF varies but less than 10.4%. This number is strongly determined by the patch shape factor, mildly influenced by the patch Reynolds number while already accounting for the SVF and number of stems in its expression and thus it is very little affected by them.

The main implications of the current study are urban channel management and ecosystem restoration. Artificial vegetation in urban waterways is beneficial for re-meandering channels and reconstruction of the flow pattern to naturally-like pool-riffle structures which favours biodiversity. Also, the associated physical (increase eddy frequency, sedimentation, erosion), chemical (accumulation, sorption) and biological (self-purification, oxygen production and denitrification) processes are also activated in man-made channels. Moreover, based on the finding of VP length scale on eddy frequency, the further studies relevant to turbulent events, such as the dispersion of suspended sediments in VP flow, the length scale of VP may have an important role besides the vegetation diameter scale and SVF.

The main limitation of the current study is that the vegetation is simplified into rigid emergent stems. The submergence and flexibility of stems are not involved in this U-bend channel study, which needs further exploration.

6. Nomenclature

A	Projection area of single stem (mm^2)
B	Width of channel (m)
C_d	Drag coefficient
$C_{d\theta}$	Bulk drag coefficients of vegetation patch in streamwise
C_{dr}	Bulk drag coefficients of vegetation patch in radius-wise (spanwise)
$C_{d\theta i}$	Time-averaged drag coefficients on each row in streamwise
C_f	Bed friction coefficient
C_l	Lift coefficient of a single cylinder
CR	Curvature ratio which is defined as R/B
d	Diameter of stems in vegetation patch (mm)
D	Diameter of vegetation patch (mm)
f_e	Local dominant eddy frequency (Hz)
f_p	Local dominant eddy frequency of vegetation patch (Hz)
f	Frequency of flow events (Hz)
F_{drag}	Drag force for a single cylinder (N)
F_{lift}	Lift force for a single cylinder (N)
F_Θ	Streamwise vegetation patch drag force (N)
F_r	Radius-wise (spanwise) vegetation patch drag force
Fr	Froude number
H	Depth of water in outlet (m)
l	Length scale (m)
L	Spanwise scale of vegetation patch (m)
Ls	Streamwise length between stems Row 1 and stems Row 10 (m)
N	Number of stems in a patch
Q	Inlet discharge rate (m^3/s)
Δr	Distance between the first node to cylinders surface (mm)
R	Inner bank radius (m)
Re	Reynolds number
Re_d	Reynolds number based on the diameter of a stem or a cylinder
Re_p	Reynolds number based on the scale of patch
RSM	Reynolds Stress Model

St_e	Dimensionless eddy frequency
St_p	Dominant dimensionless vortices' shedding frequency of vegetation patch
St_d	Vortex shedding frequency of single cylinder or stem
SVF	Solid volume fraction of a vegetation patch
u'	Streamwise velocity fluctuation (m/s)
U	Time-averaged streamwise velocity (m/s)
U_m	Inlet average velocity (m/s)
$\bar{U}$	Time-space-averaged velocity including vegetated region and non-vegetated region (m/s)
$\overline{U_1}$	The cross-section averaged streamwise velocity in vegetation region
$\overline{U_2}$	The cross-section averaged streamwise velocity in non-vegetation region
ΔU	Time-averaged velocity difference between the vegetation region and non-vegetated region (m/s)
URANS	Unsteady Reynolds Averaged Navier-Stokes method
v'	Spanwise velocity fluctuation (m/s)
W	Vertical velocity (m/s)
VOF	Volume Of Fluid method
VP	Vegetation patch
Δx^+	The streamwise dimensionless wall distance for a mesh centre
X	Streamwise direction
Δy^+	The spanwise dimensionless wall distance for a mesh centre
Y	Spanwise direction
$\bar{Y}$	A location where $U = \bar{U}$
Δz^+	The vertical dimensionless wall distance for a mesh centre
Z	Vertical direction
$St_p \frac{\sqrt{\mathrm{SVF}}}{\sqrt{N}}$	A newly proposed dimensionless frequency number accounting for the vegetation density and number of stems in the patch
ρ	Density of water (kg/m^3)
τ	Bed shear stress (pa)
θ	The momentum thickness in mixing layer (m)

7. Supplementary materials

Mesh independent tests were performed using a pair of meshes shown in Fig.3(b) and Fig.21. The Re_d based on the diameter of the single cylinder is 1000. The URANS RSM approach was selected as the turbulence model, where the RSM model constants were exactly the same as the values shown in Table 3. Second-order upwind schemes were used for the convection terms. The time marching was second order and the time steps were chosen while the maximum Courant number is less than 0.5. The residuals were less than 10^{-6} before reaching the convergence criterion in each time step.

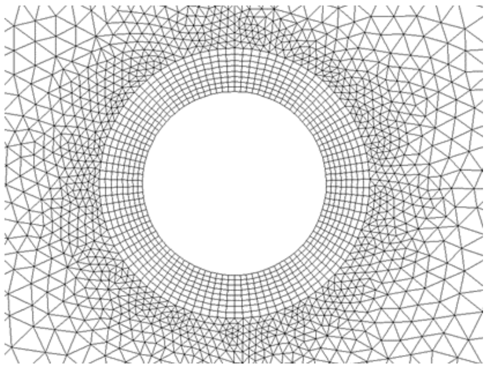

Fig.21 the refined meshes $\Delta r/d$=1/30 for the mesh independent tests, as compared to mesh shown in Fig.3(b), where $\Delta r/d$=1/15.

The drag coefficient and lift coefficient are evaluated by Eqs (13,14) (Zhang et al. 2019, Chang and Constantinescu, 2015, Nicolle, and Eames, 2011).

$$C_d = \frac{F_{drag}}{\frac{1}{2}A\rho U^2}, \tag{13}$$

$$C_l = \frac{F_{lift}}{\frac{1}{2}A\rho U^2}, \tag{14}$$

where C_d, C_l, F_{drag}, F_{lift}, A, ρ, U are the drag coefficient, lift coefficient, drag force, lift force, the front projection area, fluid density and flow velocity. The time histories of drag coefficient and lift coefficient generated by the above meshes were presented in Fig.22. Comparing results from Fig.3(b) and Fig.21, the time-averaged drag coefficients are 1.24 and 1.25, respectively. The results from mesh Fig.21 is slightly higher than that of mesh in Fig.3(b) because of the less dissipation from the higher spatial resolution mesh. However, the general results from both meshes agree well and are independent on current meshes.

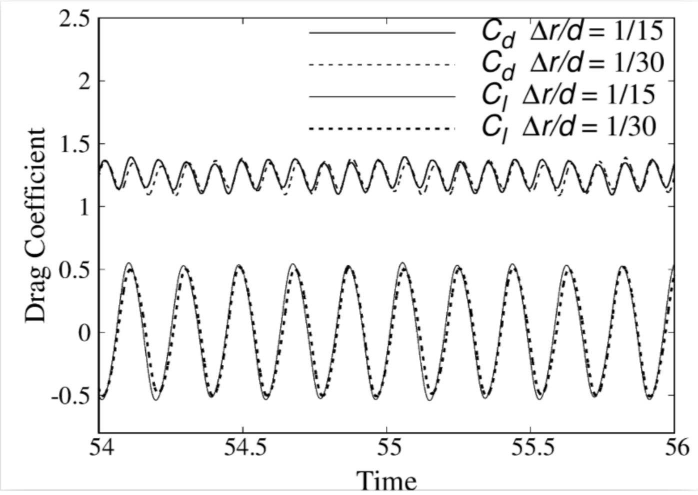

Fig.22 Drag coefficients (C_d) and lift coefficients (C_l) of a single solid cylinder predicted by URANS RSM using meshes shown in Fig.3(a) and Fig.21, where the first layer meshes are $\Delta r/d$=1/15 and $\Delta r/d$=1/30, respectively.

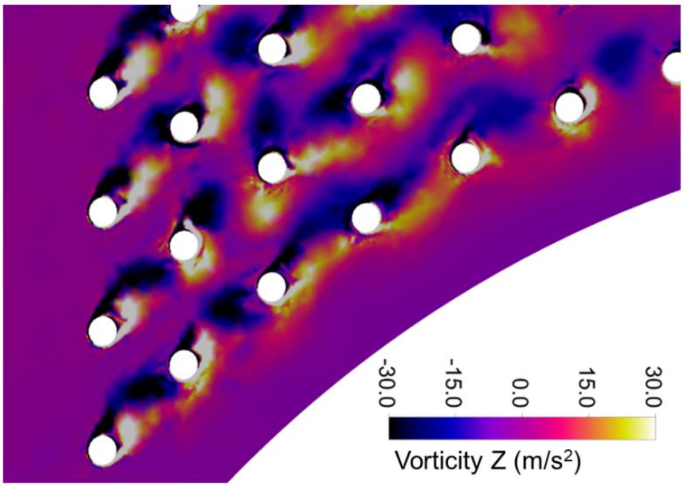

Fig.23 An instantaneous vertical vorticity contour plot to visualize the "amalgamation process", at the leading edge of the VP in the case 5 with CR=0.5 d=12.45mm SVF=4.86%.

8. Acknowledgement

The first author thanks CSC and QMUL for supporting his Ph.D. studentship. Further acknowledgement is given to the UK EPSRC Turbulence Consortium, grant EP/R02932611 and the Royal society IEC/NSFC/1181425.

9. References

ANSYS Fluent Theory Guide, 2019R1, Section 4.9 Reynolds Stress Model (RSM), 2019.

Armanini, A., and Cavedon, V., 2019. Bed-load through emergent vegetation. *Advances in Water*

Resources. doi.org/10.1016/j.advwatres.2019.05.021

Armanini, A., Righetti, M. and Grisenti, P., 2005. Direct measurement of vegetation resistance in prototype scale. *Journal of Hydraulic Research*, *43*(5), pp.481-487.

Asahi, K., Shimizu, Y., Nelson, J. and Parker, G., 2013. Numerical simulation of river meandering with self-evolving banks. *Journal of Geophysical Research: Earth Surface*, *118*(4), pp.2208-2229.

Bertoldi, W., Siviglia, A., Tettamanti, S., et al., 2014. Modeling vegetation controls on fluvial morphological trajectories. *Geophysical Research Letters*, 41(20), pp.7167-7175.

Blanckaert, K., 2011. Hydrodynamic processes in sharp meander bends and their morphological implications. *Journal of Geophysical Research: Earth Surface*, *116*(F1).

Blanckaert, K. and De Vriend, H.J., 2004. Secondary flow in sharp open-channel bends. *Journal of Fluid Mechanics*, *498*, pp.353-380.

Blevins, R. D. (1990) *Flow-Induced Vibration*, 2nd edn., Van Nostrand Reinhold.

Braza, M., Chassaing, P.H.H.M. and Minh, H.H., 1986. Numerical study and physical analysis of the pressure and velocity fields in the near wake of a circular cylinder. *Journal of fluid mechanics*, *165*, pp.79-130.

Bywater-Reyes, S., Diehl, R.M. and Wilcox, A.C., 2018. The influence of a vegetated bar on channel-bend flow dynamics. *Earth Surface Dynamics*, *6*(2), pp.487-503.

Camporeale, C., Perucca, E., Ridolfi, L., et al., 2013 Modeling the interactions between river morphodynamics and riparian vegetation. *Reviews of Geophysics*, 51(3), pp.379-414.

Caponi, F. and Siviglia, A., 2018. Numerical modeling of plant root controls on gravel bed river morphodynamics. *Geophysical Research Letters*, *45*(17), pp.9013-9023.

Chang, K. and Constantinescu, G., 2015. Numerical investigation of flow and turbulence structure through and around a circular array of rigid cylinders. *Journal of Fluid Mechanics*, *776*, pp.161-199.

Chen, S.C., Chan, H.C. and Li, Y.H., 2012. Observations on flow and local scour around submerged flexible vegetation. *Advances in Water Resources*, 43, pp.28-37.

Choi, S.U. and Kang, H., 2004. Reynolds stress modeling of vegetated open-channel flows. *Journal of Hydraulic Research*, *42*(1), pp.3-11.

Constantinescu, G., Koken, M. and Zeng, J., 2011. The structure of turbulent flow in an open channel bend of strong curvature with deformed bed: Insight provided by detached eddy simulation. *Water Resources Research*, 47(5).

Crosato, A. and Saleh, M.S., 2011. Numerical study on the effects of floodplain vegetation on river planform style. *Earth Surface Processes and Landforms*, *36*(6), pp.711-720.

Dale, A. 1996. Engineering implications of rehabilitation of urban channels. Proc. of the 7th Int. Conf. On Urban Drain., Hannover, vol.II, pp.1211–16.

Eke, E., Parker, G. and Shimizu, Y., 2014. Numerical modeling of erosional and depositional bank processes in migrating river bends with self-formed width: Morphodynamics of bar push and bank pull. *Journal of Geophysical Research: Earth Surface*, 119(7), pp.1455-1483.

Farzadkhoo, M., Keshavarzi, A., Hamidifar, H. and Javan, M., 2019. Sudden pollutant discharge in vegetated compound meandering rivers. *Catena*, *182*, p.104155.

Folkard, A.M., 2005. Hydrodynamics of model Posidonia oceanica patches in shallow water. *Limnology and oceanography*, *50*(5), pp.1592-1600.

Ghisalberti, M. and Nepf, H.M., 2002. Mixing layers and coherent structures in vegetated aquatic flows. *Journal of Geophysical Research: Oceans*, *107*(C2), pp.3-1.

Graf, W.H. and Blanckaert, K., 2002, June. Flow around bends in rivers. In *The* 2_{nd} *International*

Conference New Trends in Water and Environmental Engineering for Safety and Life: Eco-compatible Solutions for Aquatic Environments. Capri (Italy).

Gurnell, A., Thompson, K., Goodson, J. and Moggridge, H., 2008. Propagule deposition along river margins: linking hydrology and ecology. *Journal of Ecology*, *96*(3), pp.553-565.

Hamidifar, H., Keshavarzi, A. and Rowiński, P.M., 2020. Influence of Rigid Emerged Vegetation in a Channel Bend on Bed Topography and Flow Velocity Field: Laboratory Experiments. *Water*, *12*(1), p.118.

Huai, W.X., Li, C.G., Zeng, Y.H., Qian, Z.D. and Yang, Z.H., 2012. Curved open channel flow on vegetation roughened inner bank. *Journal of Hydrodynamics*, *24*(1), pp.124-129.

Huai, W.X., Xue, W. and Qian, Z., 2015. Large-eddy simulation of turbulent rectangular open-channel flow with an emergent rigid vegetation patch. *Advances in water resources*, *80*, pp.30-42.

Huai, W.X., Zhang, J., Wang, W.J. and Katul, G.G., 2019. Turbulence structure in open channel flow with partially covered artificial emergent vegetation. *Journal of Hydrology*, *573*, pp.180-193.

Jiang, H., and Cheng, L., 2017. Strouhal–reynolds number relationship for flow past a circular cylinder. *Journal of Fluid Mechanics,* 832, pp.170-188.

Jourdain, C., Claude, N., Tassi, P., Cordier, F. and Antoine, G., 2020. Morphodynamics of alternate bars in the presence of riparian vegetation. *Earth Surface Processes and Landforms*, 45(5), pp.1100-1122.

Kang, T., Kimura, I. and Shimizu, Y., 2018. Responses of bed morphology to vegetation growth and flood discharge at a sharp river bend. *Water*, *10*(2), p.223.

Kashyap, S., Constantinescu, G., Rennie, C.D., Post, G. and Townsend, R., 2012. Influence of channel aspect ratio and curvature on flow, secondary circulation, and bed shear stress in a rectangular channel bend. *Journal of Hydraulic Engineering*, *138*(12), pp.1045-1059.

Krauze, K., Zawilski, M. and Wagner, I., 2008. Aquatic habitat rehabilitation: Goals, constraints and techniques. *Aquatic Habitats in Integrated Urban Water Management*, pp.71-93.

Le Bouteiller, C., and Venditti, J. G., 2015. Sediment transport and shear stress partitioning in a vegetated flow. *Water Resources Research*, *51*(4), pp.2901-2922.

Luhar, M., Rominger, J., and Nepf, H., 2008. Interaction between flow, transport and vegetation spatial structure. *Environmental Fluid Mechanics*, *8*(5-6), pp.423.

Merritt, D.M. and Wohl, E.E., 2002. Processes governing hydrochory along rivers: hydraulics, hydrology, and dispersal phenology. *Ecological applications*, *12*(4), pp.1071-1087.

Nepf, H.M., 1999. Drag, turbulence, and diffusion in flow through emergent vegetation. *Water resources research*, *35*(2), pp.479-489.

Nepf, H.M., 2012. Flow and transport in regions with aquatic vegetation. *Annual review of fluid mechanics*, *44*, pp.123-142.

Nicholas A.P., Ashworth P.J., Smith G.H.S., et al., 2013, Numerical simulation of bar and island morphodynamics in anabranching megarivers. *Journal of Geophysical Research*, Earth Surface, 118(4), pp.2019-2044.

Nicolle, A. and Eames, I., 2011. Numerical study of flow through and around a circular array of cylinders. *Journal of Fluid Mechanics*, *679*, pp.1-31.

Okajima, A., 1982. Strouhal numbers of rectangular cylinders. *Journal of Fluid mechanics*, *123*, pp.379-398.

Ramamurthy, A.S., Han, S.S. and Biron, P.M., 2012. Three-dimensional simulation parameters for 90 open channel bend flows. *Journal of Computing in Civil Engineering*, *27*(3), pp.282-291.

Rominger, J.T., Lightbody, A.F. and Nepf, H.M., 2010. Effects of added vegetation on sand bar stability and stream hydrodynamics. *Journal of Hydraulic Engineering*, *136*(12), pp.994-1002.

Roshko, A., 1961. Experiments on the flow past a circular cylinder at very high Reynolds number. *Journal of fluid mechanics* 10(3), pp. 345-356.

Schnauder, I. and Sukhodolov, A.N., 2012. Flow in a tightly curving meander bend: effects of seasonal changes in aquatic macrophyte cover. *Earth Surface Processes and Landforms*, *37*(11), pp.1142-1157.

Schwartz, J.S., Herricks, E.E., Rodriguez, J.F., Rhoads, B.L., Garcia, M.H. and Bombardelli, F.A., 2002. Physical habitat analysis and design of in-channel structures on a Chicago, IL urban drainage: a stream naturalization design process. In *Global Solutions for Urban Drainage* (pp. 1-13).

Souliotis, D. and Prinos, P., 2011. Effect of a vegetation patch on turbulent channel flow. *Journal of Hydraulic Research*, *49*(2), pp.157-167.

Sumner, D., 2010. Two circular cylinders in cross-flow: a review. *Journal of fluids and structures*, *26*(6), pp.849-899.

Sugiyama, H. and Hitomi, D., 2005. Numerical analysis of developing turbulent flow in a 180 bend tube by an algebraic Reynolds stress model. *International Journal for Numerical Methods in Fluids*, *47*(12), pp.1431-1449.

Tennekes, H. and, Lumley, J.L., 1972. *A first course in turbulence*. MIT press. pp.28-57.

Termini, D., 2017. Vegetation effects on cross-sectional flow in a large amplitude meandering bend. *Journal of Hydraulic Research*, *55*(3), pp.423-429.

Termini, D. and Di Leonardo, A., 2018. Turbulence structure and implications in exchange processes in high-amplitude vegetated meanders: experimental investigation. *Advances in Water Resources*, *120*, pp.114-127.

Van Balen, W., Blanckaert, K. and Uijttewaal, W.S.J., 2010. Analysis of the role of turbulence in curved open-channel flow at different water depths by means of experiments, LES and RANS. *Journal of Turbulence*, (11), p.N12.

Van Dijk, W.M., Teske, R., Van de Lageweg, W.I. and Kleinhans, M.G., 2013. Effects of vegetation distribution on experimental river channel dynamics. *Water Resources Research*, 49(11), pp.7558-7574

Van Dijk, W.M., 2013. Meandering rivers-feedbacks between channel dynamics, floodplain and vegetation. *Utrecht Studies in Earth Sciences*, *35*.

Van Katwijk, M. M., Bos, A. R., Hermus, D. C. R., and Suykerbuyk, W., 2010. Sediment modification by seagrass beds: Muddification and sandification induced by plant cover and environmental conditions. *Estuarine, Coastal and Shelf Science*, *89*(2), pp.175-181.

Wang, M.Y., Avital, E., Bai, X., Ji C., Williams, J., Munjiza, A., 2019. Fluid-structure interaction of flexible submerged vegetation stems and kinetic turbine blades, *Journal of Computational Particle Mechanics*, pp.1-10.

Wei, M., Blanckaert, K., Heyman, J., Li, D. and Schleiss, A.J., 2016. A parametrical study on secondary flow in sharp open-channel bends: experiments and theoretical modelling. *Journal of hydro-environment research*, *13*, pp.1-13.

Wu, W., Shields Jr, F.D., Bennett, S.J. and Wang, S.S., 2005. A depth-averaged two-dimensional model for flow, sediment transport, and bed topography in curved channels with riparian vegetation. *Water Resources Research*, *41*(3).

Yang, Z.H., Bai, F.P., Huai, W.X. and Li, C.G., 2019. Lattice Boltzmann method for simulating flows in open-channel with partial emergent rigid vegetation cover. *Journal of Hydrodynamics*, *31*(4), pp.717-724.

Yu, G., Avital, E.J. and Williams, J.J.R., 2008. Large eddy simulation of flow past free surface piercing circular cylinders. *Journal of Fluids Engineering*, *130*(10).

Zdravkovich, M.M., 1997. Flow around circular cylinders; vol. i fundamentals. *Journal of Fluid Mechanics*, *350*(1), pp.377-378.

Zen, S., Zolezzi, G., Toffolon, M. and Gurnell, A.M., 2016. Biomorphodynamic modelling of inner bank advance in migrating meander bends. *Advances in water resources*, 93, pp.166-181.

Zhang, J., Liang, D., Fan, X. and Liu, H., 2019. Detached eddy simulation of flow through a circular patch of free-surface-piercing cylinders. *Advances in water resources*, *123*, pp.96-108.

Zimmermann, C., 1977. Roughness effects on the flow direction near curved stream beds. *Journal of Hydraulic Research*, *15*(1), pp.73-85.